

HERSCHEL SURVEY OF THE PALOMAR-GREEN QSOS AT LOW REDSHIFT

ANDREEA O. PETRIC¹, LUIS C. HO^{2,3}, NICOLAS J. M. FLAGEY⁴, NICHOLAS Z. SCOVILLE⁵*Draft version March 2, 2024*

ABSTRACT

We investigate the global cold dust properties of 85 nearby ($z \leq 0.5$) QSOs, chosen from the Palomar-Green sample of optically luminous quasars. We determine their infrared spectral energy distributions and estimate their rest-frame luminosities by combining *Herschel* data from 70 to 500 μm with near-infrared and mid-infrared measurements from the Two Micron All Sky Survey (2MASS) and the Wide-Field Infrared Survey Explorer (WISE). In most sources the far-infrared (FIR) emission can be attributed to thermally heated dust. Single temperature modified black body fits to the FIR photometry give an average dust temperature for the sample of 33 K, with a standard deviation of 8 K, and an average dust mass of $7 \times 10^6 M_\odot$ with a standard deviation of $9 \times 10^6 M_\odot$. Estimates of star-formation that are based on the FIR continuum emission correlate with those based on the 11.3 μm PAH feature, however, the star-formation rates estimated from the FIR continuum are higher than those estimated from the 11.3 μm PAH emission. We attribute this result to a variety of factors including the possible destruction of the PAHs and that, in some sources, a fraction of the FIR originates from dust heated by the active galactic nucleus and by old stars.

Keywords: AGN, galaxy evolution

1. INTRODUCTION

Insight into the properties and evolution of the interstellar medium (ISM) is critical for building theories of how galaxies evolve. The ISM is the birthplace of stars, is enriched by them, and feeds super-massive black holes (BH). Galaxies evolve by transforming their gas and dust reservoirs into stars at low rates, through occasional dramatic interactions, and by capturing gas and stars from the intergalactic medium.

The consequence of those events appears to be that the masses of central BH are correlated with the stellar mass and velocity dispersion of the bulge. This was suggested by observations of the dynamics of stars and gas in the nuclear regions of nearby galaxies (e.g. Magorrian et al. 1998; Ferrarese & Merritt 2000; Gebhardt et al. 2000; Tremaine et al. 2002; Kormendy & Ho 2013, and references therein).

A frequently offered explanation for this correlation is that the bulge and the BH control each other's growth through their interactions with the ISM. AGN winds and/or jets impact the gas and dust in the surrounding ISM (i.e. feedback). The AGN radiation can heat, ionize and/or push out the ISM; this quenches star-formation and limits the amount of fuel available for accretion into the BH. AGN related activity such as powerful radio jets can also have the opposite effect, that is, jets drive shocks through the ISM, create regions of compressed gas facilitating enhanced star-formation. Kormendy & Ho (2013) show that differences between the light profiles of ellip-

ticals can be related to the type of AGN feedback they experienced. To test models of how AGN affect the ISM we need an accurate census of the ISM in AGN hosts as a function of AGN properties.

One practical method to estimate the mass of cold ISM is to measure the total dust mass and then use an appropriate gas-to-dust ratio to infer the total cold ISM. In this paper we focus on the first step: measure the FIR emission and assess whether it is thermal dust emission in star-forming regions.

Observations in the FIR of large samples of nearby, luminous, broad-line QSOs were done with the Infrared Astronomical Satellite (IRAS) by Neugebauer et al. (1986) and Sanders et al. (1988a). Sanders et al. (1988a,b) suggested that QSOs were preceded by a dusty ULIRG phase. Haas et al. (2003) observed a sample of 64 PG QSOs with the *Infrared Space Observatory* (ISO) satellite and suggested that the observed diversity of SEDs implied changes in the dust distribution as the host galaxies evolved. Pre-ALMA studies of molecular and neutral gas emission (Evans et al. 2001; Scoville et al. 2003; Bertram et al. 2007; Ho et al. 2008) made it clear that a significant fraction of optically selected quasars have considerable amounts ($\sim 10^9 - 10^{10} M_\odot$) of cold gas.

With unprecedented high resolution and sensitivity, the European Space Agency's *Herschel Space Observatory* (Pilbratt et al. 2010) dramatically increased our ability to measure the ISM of nearby and higher redshift sources (e.g. Lutz 2014). Here we present measurements of cold dust in a sample of 85 of the 87 nearby ($z \leq 0.5$), optically luminous, broad-line QSOs selected from the Palomar Bright Quasar Survey Catalogue of Schmidt & Green (1983) with redshifts from Boroson & Green (1992)⁶

The QSOs targeted in this FIR survey have BH masses

¹ Gemini Observatories, 670 N. A'Ohoku Pl., Hilo, HI, 96720, USA

² Kavli Institute for Astronomy and Astrophysics, Peking University, Beijing 100871, China

³ Department of Astronomy, School of Physics, Peking University, Beijing 100871, China

⁴ Institute for Astronomy, 640 North A'Ohoku Place, Hilo, HI 96720, USA

⁵ California Institute of Technology, 1200 E. California Blvd., MS 249-17, 91125, USA

⁶ We only present FIR photometry for 85 out of the 87 sources in the (Boroson & Green 1992) sample because we shared several targets with other Herschel programs, which were not completed.

in the range of known BH masses (M_{BH}) from $\sim 10^{6.5}$ to $10^{9.5} M_{\odot}$ and L_{bol}/L_{Edd} from 0.03 to 1 (Boroson 2002). Multi-wavelength studies from X-ray to radio (e.g. Elvis et al. 1986; Bechtold et al. 1987; Kellermann et al. 1989; Evans et al. 2001; Scoville et al. 2003; Guyon et al. 2006; Dasyra et al. 2007; Veilleux et al. 2009) help place the Herschel observations in a wider astrophysical context.

We compare FIR observations to radio and MIR data to investigate the origin of the FIR. We use the radio observations to estimate how much of the observed FIR could be synchrotron radiation in addition to thermal dust emission.

We also compare the FIR continuum to PAH emission since both trace star-formation. The FIR emission is mostly large grains ($> 0.1 \mu m$) that absorb and re-radiate starlight emission and PAH emission originates from organic compounds excited by optical/UV radiation from young stars. PAH emission is weaker in local AGN than in star-forming regions (Roche et al. 1991) but PAH studies of AGN samples disagree about the reliability of SFR estimates from PAHs. LaMassa et al. (2012) finds that the luminosity of the $11.3 \mu m$ feature is significantly suppressed relative to other PAH features in AGN dominated systems, while Diamond-Stanic & Rieke (2010), Diaz-Santos et al. (2010) and Esquej et al. (2014) find that the $11.3 \mu m$ PAH feature can survive within 100 pc from the AGN and that for nearby Seyferts the $11.3 \mu m$ PAH is not suppressed.

The paper is structured as follows: in section 2 we describe the observational setup and data reduction, in section 3 we present basic photometric results and basic derivations of rest frame luminosities, spectral indices and global dust masses and temperatures. In section 4 we analyze the dust masses and temperatures relative to the radio and PAH $11.3 \mu m$ properties and in section 5 we summarize our findings and conclusions.

2. OBSERVATIONS AND DATA ANALYSIS

The photometric data presented here were taken with the *Herschel Space Observatory* (Pilbratt et al. 2010). Our observations employed the Photodetector Array Camera and Spectrometer (PACS, Poglitsch et al. 2010) and the Spectral and Photometric Imaging Receiver (SPIRE, Griffin et al. 2010) instruments. With PACS we measured the 70, 100, and $160 \mu m$ broadband emission and with SPIRE the 250, 350 and $500 \mu m$ emission.

2.1. PACS

The PACS observations were performed in the *mini-scan mode* with scan angles of 70 and 110 degrees, as recommended by the instrument team. Our scanning speed was $20''/\text{sec}$. PACS is a dual photometer allowing simultaneous short wavelength (70 or $100 \mu m$) and long wavelength ($160 \mu m$) observations over a field of view of $1.75' \times 3.5'$. The FWHMs of the PSF are $5.46'' \times 5.76''$, $6.69'' \times 6.89''$, and $10.65'' \times 12.13''$ ⁷. The integration time for each scan angle was 180 seconds.

We processed all the PACS data using the pipeline in the Herschel Interactive Processing Environment (HIPE) and associated calibrations version 48 and above. Details

of the HIPE pipeline and calibration tables are presented in the online PACS data reduction manual⁸.

We combine the two PACS scans into a final image employing standard North - America Herschel Science Center (NHSC) data reprocessing tools combined in a script provided by the NHSC PACS team. The pixel sizes of the 70, 100 and $160 \mu m$ maps are 1.2, 1.4, and $2.1''$. These pixel sizes were used by the PACS team in maps of calibration sources to adequately sample the PSF.

The PACS fluxes presented here are computed by summing all pixels within circular $\sim 20''$ apertures centered at the centroids of the 70, 100, and $160 \mu m$ emission, respectively. For some targets we adjusted slightly the aperture size, if there was another source or a bad pixel near the source. The background was estimated from the median value of apertures placed throughout the map, avoiding positions which would include the source. We fit the distribution of fluxes in those apertures with a gaussian plus a second order polynomial. The second-order polynomial is needed to model the higher noise at the map edges. We choose the median value of the distribution of background apertures fluxes as our final background estimate noting that the median value is within a few percent of the mean value for most maps.

We estimate flux measurements errors (σ) from the standard deviation of the gaussian used to fit to the distribution of background aperture fluxes. Upper limits are 3σ . We then apply the aperture correction factors provided in the official PACS documentation. The aperture corrections range between 1.1 and 1.3, 1.1 and 1.3, and 1.1 and 1.2 at $70 \mu m$, $100 \mu m$, and $160 \mu m$ respectively. The flux calibration accuracy of PACS observation is 5%.

2.2. SPIRE

The SPIRE observations were taken in *small-scan-map mode*. SPIRE has an effective field of view of $4' \times 8'$. The PSF FWHMs for the SPIRE data are $18.1''$, $25.2''$, and $36.6''$ respectively. The SPIRE maps have pixel sizes of $6''$, $8''$, and $12''$ at 250, 350, and $500 \mu m$, respectively. The duration of each on-source integration was 37 seconds.

The SPIRE fluxes are estimated following the suggestions from the SPIRE instrument team (Pearson et al. 2013). The Herschel/SPIRE photometer's most basic data products are timeline data (Griffin et al. 2010). These data contain information about each of the bolometers including their positions, and voltage registered at each position as they scan a source⁹. The SPIRE-ICC (Instrument Control Center) and both the North - America and the ESA Herschel Science Centers recommend fitting the timeline data to estimate the fluxes of unresolved sources¹⁰.

The PSF fitter routine provided in HIPE fits a Gaussian to the signal versus position timeline data. For unresolved sources, the peak of the fitted Gaussian corresponds to the flux density of the source. This procedure is also employed to derive the flux calibration parameters for SPIRE observations Bendo et al. (2013).

The SPIRE Timeline fitter uses a Levenberg-

⁸ http://herschel.esac.esa.int/Data_Processing.shtml

⁹ http://herschel.esac.esa.int/twiki/pub/Public/DataProcessingWorkshop40/04_SPIRE_0120.pdf

⁷ See: <http://herschel.esac.esa.int/twiki/pub/Public/PacsCalibrationTables/PacsCalibrationManualSection5.2.11>

Marquardt algorithm to fit all the timeline data associated with one source and avoid smearing effects due to pixelization associated with the SPIRE map-making process. The timeline fitter requires default values for how far from a given source position it should search for a flux peak, and also what annulus outside this region it can use to estimate the background. The default values for those parameters were derived from observations of Neptune and Gamma Draconis (Bendo et al. 2013) and tested with observations of standard calibration stars.

The uncertainties in the fluxes we present at 250, 350 and 500 μm are the errors from the timeline fitter. SPIRE flux calibration uncertainties are estimated to be $\sim 7\%$ (Bendo et al. 2013). For non-detections we calculate upper limits as 3 times the standard deviation in the timeline data. The SPIRE errors are consistent with the confusion limit fluxes estimated by Nguyen et al. (2010).

We test visually that the sources we deem as detections using the timeline fitter are not affected by the presence of other objects by producing maps and comparing the SPIRE sources visible in these SPIRE maps with sources that are visible in the higher resolution PACS maps.

3. RESULTS

3.1. Measurements

Flux measurements and associated basic statistics are given in Tables 1 and 2. The *Herschel* data have more than an order of magnitude higher spatial resolution than previous IRAS observations and a factor of 8 better than those from ISO and we are able to detect sources that are about 4 times fainter than the faintest PG QSOs detected by IRAS and ISO. Figure 1 shows histograms of the measured fluxes at 70, 100, 160, 250, 350, and 500 μm .

NIR and MIR from the Two Micron All Sky Survey (Skrutskie et al. 2006, 2MASS) and Wide-field Infrared Survey Explorer (Wright et al. 2010, WISE) surveys are given in Table 3. We obtained those by searching the IRSA catalogs within a radius of 15" of the optical position. This search radius was chosen to be comparable to the 12" angular resolution of the 22 μm WISE observations and include potential WISE pointing errors. Two examples of the NIR through FIR SEDs are plotted in Figure 2. The electronic version presents the SEDs for all the 85 targets.

Most SEDs peak at $\sim 100 \mu\text{m}$, (Figure 2) suggesting that the observed FIR is thermal emission from cold ($\sim 40\text{K}$) dust. The shapes of most SEDs are modified black-bodies, therefore we fit modified black bodies to the FIR data (see section 3.4). The error bars of the NIR and MIR fluxes, are also plotted but are significantly smaller than the relative FIR errors. In appendix A2 we investigate the radio properties of the PG SOs to estimate the amount of synchrotron radiation which contributes to the observed FIR emission in radio loud PG QSOs. Ancillary radio data at 1.4 and 5 GHz suggest that in 8% of the sources the emission at wavelengths longer than 250 μm may contain synchrotron emission associated with radio loud AGN activity.

3.2. Comparison with previous measurements

In this section we compare the *Herschel* photometry with previous measurements.

3.2.1. ISO 100 μm

Figure 3 compares 31 PG QSOs observed with both *Herschel* and ISO at 100 μm . Measurements are consistent within detection sensitivities. Two sources have ISO fluxes that are much lower than the *Herschel* measurements. Among those, on target was also observed at 70 μm with MIPS and the *Herschel* flux is within 5% of the MIPS flux. In sum, Figure 3 illustrates that at the bright end the ISO and *Herschel* fluxes agree very well and at the faint end the *Herschel* observations are factor of few to a magnitude more sensitive.

3.2.2. Spitzer MIPS 70 μm

In figure 3 we also compare our measurements to those from MIPS (Shi et al. 2014). The PACS photometry presented in this paper are consistent on average with the MIPS observations, but have higher resolution (e.g. at 160 μm SPITZER MIPS has a resolution of while *Herschel* PACS images have a spatial resolution of)

3.2.3. MIPS and Herschel 160 μm

Shi et al. (2014) present *Herschel* PACS and Spitzer MIPS 160 μm measurements for 78 of the 85 PG QSOs we present here. Figure 3 shows those are consistent with the values in this work.

3.3. Rest Frame Luminosities

WISE observations at 5.5, 8 and 24 μm are combined with *Herschel* 70, 100, 160, 250, 350 and 500 μm data to estimate rest-frame luminosities at several key wavelengths, i.e. wavelengths that are often used to characterize the MIR and FIR properties of galaxy samples. This was done as follows: for each observed flux we determine the corresponding rest-frame $\lambda_{rest} = \lambda_{obs}/(1+z)$ and then compute the $F_{\lambda_{rest}}$ flux. We then derive spectral indices ($\alpha : F_{\lambda} \propto \lambda^{\alpha}$) from each pair of adjacent spectral measurements. Finally we use these spectral indices to estimate the rest-frame fluxes at rest-frame 5.5, 8, 24, 60, 70, 100, 160, 250, 350, and 500 μm .

We list rest-frame luminosities emitted at 5.5, 8, 24, 60, 70, 100, 160, 250, 350, and 500 μm in Table 4, and show histograms of rest frame luminosities at 60, 100, 160, 250, 350 and 500 μm in Figure 4. We present basic statistics in Table 5: minimum, maximum, median luminosities, and the medians of the distributions including the upper limits derived using the Kaplan Meier estimators¹¹. The PG QSOs span a wide range of IR luminosities from values comparable to the IR luminosities of normal galaxies to those of Ultraluminous Infrared Galaxies (ULIRGs), which is consistent with previous findings (e.g. (Haas et al. 2003))

In Table 4 we also present FIR luminosities, from 40 to 500 μm and the 42.5 to 122.5 μm FIR (e.g. Helou et al. 1985; Condon 1992):

$$\left(\frac{FIR}{W m^{-2}} \right) = 1.26 \times 10^{-14} \left(\frac{2.58 S_{60\mu m} + S_{100\mu m}}{Jy} \right) \quad (1)$$

where $S_{60\mu m}$ and $S_{100\mu m}$ are the flux densities in rest frame at 60 and 100 μm .

¹¹ as implemented in the statistics package *R* (Feigelson & Jogesh Babu 2012)

3.4. SED templates

Composite SEDs are frequently used to compare different populations of objects, to study their evolution, and to assess whether selecting specific sources in one wavelength regime biases our understanding of their properties at other wavelengths. (e.g. Boyle 1990; Cristiani & Vio 1990; Francis et al. 1991; Elvis et al. 1994; Zheng et al. 1997; Brotherton et al. 2001; Vanden Berk et al. 2001; Telfer et al. 2002; Scott et al. 2004; Glikman et al. 2006; Hanish et al. 2013).

In this paper we present a template combining SEDs of nearby, optically luminous, broad-line QSOs, normalized at $6\ \mu\text{m}$ (Figure 5). We combine the SEDs as follows: (1) we bin the rest-frame fluxes estimated from each observed photometric band, and then (2) we compute the median, and the 95% confidence intervals using the Kaplan-Meier estimator. We present those in table 6. We speculate that the heterogeneity in observed FIR properties may be connected to a variety of evolutionary paths for these sources and that the hosts of galaxies evolve slower than the central accreting SMBH, because the emission most closely associated with the AGN and the torus (i.e. optical and NIR fluxes) are fairly homogeneous.

Substantial effort has recently been put in using rest-frame far-infrared emission as a tracer of star-formation in high redshift AGN. This relies on the FIR in those systems typically not being strongly contaminated by AGN heated emission. One way to support this semi-quantitatively is by comparison to intrinsic AGN SEDs typically derived by decomposing AGN SEDs and host with the aid of Spitzer spectroscopy. The most common AGN SEDs of this type are by Netzer et al. (2007) and Mullaney et al. (2011). In Figure 6 we compare the median SEDs derived from the PG QSOs to the average observed SED of 28 PG QSOs observed with IRS from Netzer et al. (2007) and to the average SED of 8 FIR-weak PG QSOs from which the starburst component was subtracted Netzer et al. (2007). We also compare the template from the data presented in this paper to the average SEDs of nearby AGN with high and low luminosities, i.e. with $\log(L_{2-10\text{keV}}) \geq 42.9$ respectively) from Mullaney et al. (2011). The templates from Netzer et al. (2007) and Mullaney et al. (2011) seem to have relatively higher MIR emission originating from the AGN and lower FIR emission than the template presented here from WISE and Herschel photometry. This difference is maintained but slightly reduced if we exclude radio loud QSOs from our sample as well as AGN with $S_{350\mu\text{m}} \geq S_{250\mu\text{m}}$. These differences suggest that the templates Netzer et al. (2007) and Mullaney et al. (2011) represent sources with hotter dust, or smaller grains emitting in the MIR. As shown in Figure 6 starburst galaxy templates as derived by Mullaney et al. (2011) have comparatively more large old grains emitting in the FIR. Note that both Netzer et al. (2007) and Mullaney et al. (2011) estimated the intrinsic AGN-only template. We leave a similar, more detailed analysis of the MIR and FIR data for a future investigation.

3.5. Dust Mass and Temperature Estimates

Dust masses and temperatures are estimated from single temperature modified black-body fits to the far-IR SEDs, i.e. including all the PACS and SPIRE photometry ($70\text{--}500\ \mu\text{m}$). The results are presented in Table 7. It has been known for decades that there are multiple types of grain populations, with different size distributions and chemical compositions. While small grains are stochastically heated and significantly contribute to the emission at wavelengths shorter than $\sim 70\ \mu\text{m}$ (Compiègne et al. 2010), larger grains usually emit like a modified black-body at an equilibrium temperature and dominate the emission at longer wavelengths, i.e. we only use flux measurements observed at wavelengths equal and longer than $70\ \mu\text{m}$. The far-IR emission can be used to derive an average effective temperature and a total mass for large dust particles, although for certain sources it is possible that even the $70\ \mu\text{m}$ emission comes from hotter dust associated with the AGN.

Bianchi (2013) compare different methods to derive dust masses and temperatures by fitting the far-IR SEDs with (1) a single temperature modified black body, (2) a dust emission model, i.e. assuming a combination of different grains populations, the details of these grain models being beyond the scope of this paper. Bianchi (2013) used two dust models: that of Draine & Li (2007) and that of Compiègne et al. (2011). Both of these models have been used intensively in the analysis of Spitzer and Herschel data, from nearby to high redshift sources. Bianchi (2013) find that the three estimated dust masses are within 20% of each other. He concludes that his investigation vindicates the use of the single temperature modified black body to estimate global cold dust properties in large samples of objects. However, he emphasizes the importance of using dust absorption coefficients consistent with the emissivity spectral indices used in the modified blackbody fits.

In this paper, we follow the recommendations of Bianchi (2013): we use modified blackbody fits, with absorption coefficients and spectral indices derived from the dust model of Compiègne et al. (2011) or that of Draine & Li (2007). We use both models to assess the uncertainties and systematics within our sample. We thus assume that $\kappa = \kappa_0 \left(\frac{250\mu\text{m}}{\lambda}\right)^\beta$ with $\kappa_0 = 5.01\ \text{cm}^2\text{g}^{-1}$ with an emissivity spectral index $\beta = 1.91$ inferred from the model of Compiègne et al. (2011), or $\kappa_0 = 4\text{cm}^2\text{g}^{-1}$ with an emissivity spectral index $\beta = 2.08$ from the model of Draine & Li (2007).

For optically thin dust emission with a single temperature the dust mass is given by:

$$M_d = \frac{S_{\nu_r} \times D_L^2}{\kappa_d(\nu_r) \times B(\nu_r, T_d)} \quad (2)$$

where ν_r is the rest-frame frequency, D_L is the luminosity distance estimated assuming the standard concordance cosmology and the redshifts from Boroson & Green (1992), and $B(\nu_r, T_d)$ is the Planck function at the dust temperature derived from the fit. For a source at redshift z , S_{ν_r} and $\kappa_d(\nu_r)$ are given, as a function of the observed fluxes S_{ν_o} and wavelengths λ_o , by:

$$S_{\nu_r} = \frac{S_{\nu_o}}{(1+z)} \quad (3)$$

$$\kappa_d = \kappa_0 \left[\frac{250 \mu m}{\lambda_o / (1 + z)} \right]^\beta \quad (4)$$

The quality of each fit is assessed by computing the χ^2 (Table 7). We also visually check that there are enough data points at wavelengths shorter and longer than the peak to constrain the dust temperature as shown in (Figure 7).

Global dust temperatures and masses are estimated for 72 sources. The mean and median temperatures are ~ 33 and ~ 35 K respectively and the mean and median masses are $\sim 7 \times 10^6 M_\odot$ and $\sim 3 \times 10^6 M_\odot$ respectively. The distributions of dust masses and temperatures are shown in Figure 8.

Systematic differences are found between the fits to the SEDs that use the grain properties of Compiègne et al. (2011) and those using the emissivity spectral index and dust absorption coefficient based on Draine & Li (2007). The dust temperatures are almost systematically larger by 1-2 K for the former. Consequently, the dust masses are systematically larger by about 20-40% when using the dust properties from Draine & Li (2007). This disagreement is slightly larger than that observed by Bianchi (2013). Finally, the derived χ^2 is 10-30% lower when using the β and κ from Compiègne et al. (2011). We therefore choose to present the dust masses and temperatures estimated assuming the grain properties from Compiègne et al. (2011). The disagreement between the two comes directly from the differences in κ and β .

The PG QSOs host galaxies appear to have dust masses and temperatures similar to those of nearby ellipticals but smaller than those of nearby star-forming galaxies (Figure 9). Smith et al. (2012) use Herschel observations to estimate dust masses for 62 nearby early type galaxies (ETGs). The ETGs in the Smith et al. (2012) sample have stellar masses between $\sim 10^{10}$ and $\sim 10^{11.5} M_\odot$ and are the most massive galaxies out of 322 from a volume limited sample of ETGs. We also compare our cold dust mass estimates to those of nearby star-forming galaxies which have stellar masses between from $\sim 10^{6.4}$ and $\sim 10^{11.4} M_\odot$ Skibba et al. (2011) after dividing their value by 2.7 as suggested by Bianchi (2013). This is to correct for the inconsistency between the β they derive from the fitting and the β they use to compute κ_d . Statistical tests including upper limits in our sample indicate that the dust masses of nearby galaxies (spirals and ellipticals) are somewhat different than those of PG QSOs with probability that they are the same of 11-12 %. The Kaplan Meier derived medians of $\log(M_D)$ for nearby Spirals, the PG QSO sample and elliptical galaxies are $6.8^{+0.2}_{-0.3}$, $6.6^{+0.2}_{-0.2}$, and $6.4^{+0.4}_{-0.2}$. The wide ranges of stellar masses for the different samples, as well as the non-identical ways to estimate $\log(M_D)$ upper-limits of the different samples make this comparison somewhat inconclusive.

4. DISCUSSION

In this section we discuss the origin of the FIR emission in PG QSOs and speculate about the star-formation properties of their host galaxies. We also discuss a subset of PG QSOs whose IR emission was thought to come only from AGN because IRAS and ISO did not detect them.

4.1. FIR emission and star-formation rates

We estimate star-formation rates (SFRs) from the FIR luminosities using the formulae from Murphy et al. (2011). The estimated SFRs are between ~ 0.4 and $\sim 300 M_\odot/\text{yr}$ and are correlated with the dust masses, with a 0.6 Spearman's rank correlation coefficient and a probability of 10^{-7} that they are not correlated (Figure 10). The coldest dust components dominate the estimates of total dust masses while smaller amounts of warm dust can be responsible for the the bulk of the observed FIR luminosities (Haas et al. 2003). If we assume that the dust grains size distribution is roughly the same throughout the sample, the strong correlation between the FIR luminosities, or star-formation rates derived from the FIR luminosities, and the dust masses suggests a uniform heating efficiency throughout the sample which may mean that stars are the main sources heating the dust. However the lack of a very strong correlation (i.e. a Spearman correlation coefficient larger than 0.8) could be explained by the presence of additional dust components at other temperatures or multiple sources of heating.

Star-formation rates estimated from the FIR emission are compared with SFRs derived from $11.3 \mu\text{m}$ PAH features using the measurements of Shi et al. (2007) and the formulae of Diamond-Stanic & Rieke (2010). The SFRs derived from the IR continuum correlate well with those estimated from $11.3 \mu\text{m}$ PAH (Figure 11). A Spearman rank test gives a correlation index of 0.9 with a $\sim 10^{-5}$ probability that these two quantities are not correlated. SFR rates from the PAH emission (SFR_{PAH}) are lower, on average, by a factor of 3 than those estimated from the FIR emission (SFR_{FIR}). Sources at the lowest and highest FIR luminosities show the largest differences between SFR_{FIR} and SFR_{PAH} . Out of the 22 sources with FIR luminosities above $10^{11} L_\odot$ only 8 have detectable emission at $11.3 \mu\text{m}$.

Some of the FIR emission may be processed dust heated by the AGN and associated with a clumpy torus. The $11.3 \mu\text{m}$ PAH may also trace only a fraction of the total star-formation. One example where this may take place is in the merging luminous infrared galaxy system II Zw 96 Inami et al. (2010). In this source a region of a few kpc emits $\sim 80\%$ of the IR emission of the entire system. In this region, X-ray, NIR and MIR spectroscopic diagnostics all fail to detect an AGN, although the $6.2 \mu\text{m}$ PAH EW is only half of the typical value measured in normal star-forming galaxies. Finally a significant contribution to the FIR may come from dust heated by old stars (Kennicutt & Evans 2012; Lutz 2014, e.g.) which emit fewer UV/optical photons capable to excite the PAHs.

The reliability of the $11.3 \mu\text{m}$ PAH feature as star-formation estimator in galaxies that host powerful AGN is uncertain. Esquej et al. (2014) found that the $11.3 \mu\text{m}$ PAH is not suppressed in the vicinity of low luminosity AGN while LaMassa et al. (2012) found that the $11.3 \mu\text{m}$ PAH feature is significantly suppressed in the most AGN-dominated systems. The PAH observations of Shi et al. (2007) were acquired with Spitzer IRS, and it is possible that the IRS projected slit missed some of the star-forming clumps that may significantly contribute to the FIR emission of the entire system. However, if this

were true for a significant number of sources we would find a wider range of ratios of the PAH to the FIR luminosities throughout the sample. We note however that the Diamond-Stanic & Rieke (2010) relation between the $11.3\ \mu\text{m}$ PAH feature and SFR was derived for normal spiral galaxies. Netzer et al. (2007) found that the ratios of $7.7\ \mu\text{m}$ PAH to the FIR emission in PG QSOs are similar to those measured in ULIRGs, and that those ratios are lower for ULIRGs than they are for spiral galaxies.

We speculate that FIR weak sources may also have a lower number of UV photons to excite the PAHs. At high FIR luminosities there may be an enhancement of UV and optical AGN radiation which ionizes and/or destroys the PAHs. The observed FIR may be a combination of dust heated by young and old stars, as well as dust heated by the AGN. The estimated PG QSO's dust temperatures are similar to those of normal and star-forming galaxies which may suggest that the relation between SFR and dust masses is not sufficient to disentangle the processes and sources heating the FIR emitting dust.

4.2. FIR weak QSOs

The star-formation history of the universe has been studied through many methods, including IR source counts. To disentangle between the AGN/starburst contribution to the IR luminosity, one can compare the IR slope and/or IR emission lines flux ratios to those measured for pure starbursts and pure AGN (e.g. Armus et al. 2007; Veilleux et al. 2009; Petric et al. 2011).

Eight PG QSOs have been used to represent sources in which AGN contributes 100% of the MIR emission because they were not detected by ISO and IRAS in the FIR (Netzer et al. 2007; Veilleux et al. 2009, e.g.). In this work we find that some of these PG QSOs observed with the more sensitive *Herschel* have detectable cold dust. Out of these 8 PG QSO, 5 are in our sample: PG 0026+129, PG 1309+355, PG 0923+201, PG 1617+175, PG 2251+113. All five were detected at 70 and 100 μm .

5. CONCLUSIONS

We present high sensitivity observations taken with the *Herschel Space Observatory* to measure the cold dust content in a sample of 85 nearby ($z \leq 0.5$) QSOs chosen from the optically luminous broad-line Palomar Green (PG) QSOs sample. We detect 93% of the sources in at least one *Herschel* band. The 70 μm detections range between 14 mJy and 2.3 Jy. We derive spectral indices and rest-frame luminosities at 5.5, 24, 60, 70, 100, 160, 250, 350 and 500 μm as well as FIR luminosities. The FIR luminosities span four orders of magnitude between $2 \times 10^9 L_\odot$ and $1.65 \times 10^{12} L_\odot$, i.e. between the FIR luminosities of normal galaxies to those of Ultra Luminous

Infrared Galaxies.

We combine *Herschel* data with near-infrared and mid-infrared measurements from the Two Micron All Sky Survey (2MASS) and the Wide-Field Infrared Survey Explorer (WISE) to determine their IR spectral energy distributions and to assess aggregate dust properties for 80% of the sample. We also derive an SED template normalized at 5.5 μm .

We employ single temperature modified black-body fits using two models for the dust emissivity spectral index and dust absorption coefficients from (Draine et al. 2007) and (Compiègne et al. 2011), to estimate dust temperature with a mean, median and standard deviation of 33, 35 and 8 K, and dust masses M_d with a median, mean, and standard deviation of $3, 7 \times 10^6 M_\odot$ with a standard deviation of $9 \times 10^6 M_\odot$.

We investigate how FIR indicators of star-formation compare to the $11.3\ \mu\text{m}$ PAH line as measured by (Shi et al. 2007). We find a tight correlation between the two star-forming indicators, and also between the luminosity and EW of the $11.3\ \mu\text{m}$ PAH feature and M_d . The ratios between the SFR rate from the FIR to that from the PAH range between 1.5 and 22, with median and mean values of 8 and 9 respectively. We find fairly constant ratios of the $11.3\ \mu\text{m}$ PAH luminosities to the FIR luminosities. However, at the highest FIR luminosities the ratio of the $11.3\ \mu\text{m}$ PAH to the total FIR decreases in a non-linear fashion and no $11.3\ \mu\text{m}$ PAH features were detected in sources with estimates of $T_d > 50\text{K}$. We suggest a variety of factors that may have produced those results including that in some of the FIR brightest sources, the PAHs are being destroyed by the AGN.

ACKNOWLEDGEMENTS

LCH acknowledges support by the Chinese Academy of Science through grant No. XDB09030102 (Emergence of Cosmological Structures) from the Strategic Priority Research Program and by the National Natural Science Foundation of China through grant No. 11473002.

We thank the anonymous referee for providing valuable comments and help in improving the contents of this paper.

This publication makes use of data products from the Two Micron All Sky Survey, which is a joint project of the University of Massachusetts and the Infrared Processing and Analysis Center/California Institute of Technology, funded by the National Aeronautics and Space Administration and the National Science Foundation.

AP would like to thank Mia U. and Maya Angelou for their lives and words "You may encounter many defeats, but you must not be defeated. In fact, it may be necessary to encounter the defeats, so you can know who you are, what you can rise from, how you can still come out of it" (M. A.).

APPENDIX

A1: NOTES ON INDIVIDUAL OBJECTS

PG 0007+106 The SPIRE fluxes measured in this source were higher than what would be expected from a modified black body that fits well the PACS emission (see section 3.4). We compared the centroids of the PACS and SPIRE emission regions and found them to be identical within the resolution of the data. Also the SPIRE fluxes obtained from fits to the time-line data are similar to those found with aperture photometry on the SPIRE maps. This source however is radio loud and variable, and some of the observed FIR emission may be synchrotron.

PG 0049+171 We present the measurement as a detection albeit with a large uncertainty in the given measurement

because we do see a source in the map. PG 0049+171 is not detected by IRAS at 60 μm , the quoted IRAS measurement at 60 μm is $16 \text{ mJy} \pm 77 \text{ mJy}$ comparable to the Herschel photometry at 70 μm of $45 \pm 16 \text{ mJy}$. However at 100 microns, the IRAS flux was measured at $642 \pm 280 \text{ mJy}$ (Serjeant & Hatziminaoglou 2009). Such high flux may be due to the large IRAS beam¹² which may include emission from a source 57 arcseconds away from PG 0049+171.

PG 0804+761 There are two other sources in the PACS 70 μm maps within 40" of PG 0804+761's optical position. As such the high spatial resolution Herschel photometry presented here differs from previous estimates obtained from lower angular resolution data. In particular the ISO 60 μm flux measured for this source in a 45" aperture is $188 \pm 56 \text{ mJy}$, while that from MIPS at 70 μm in an 18" aperture is $110 \pm 22 \text{ mJy}$, closer to the value of $143 \pm 13 \text{ mJy}$ from Herschel. At 100 μm the ISO flux, also measured in a 45" aperture, which very likely included at least one of the two other spurious sources, is $121 \pm 40 \text{ mJy}$, double the value of our estimate of $63 \pm 13 \text{ mJy}$. ISO did not detect the object at 200 μm but MIPS did at 160 μm with a value of $33 \pm 6.6 \text{ mJy}$ within a beam of 40" (Marshall et al. 2007). Our PACS 160 measurement is $32 \pm 8 \text{ mJy}$ after applying the aperture correction associated with an aperture of 32". The ISO fluxes were obtained via NED from Haas et al. (2003).

PG 1048-090 This source is detected in all *Herschel* bands except at 160 μm . Our measurements at 70 μm agree with those from MIPS 70 as is our upper limit at 160 microns. At 160 μm there are two faint sources, neither of which are coincident with the optical source position within one PSF. A curve of growth estimate centered on the optical position of PG 1048-090 suggests a flux on the order of 7.5 mJy, or about 1.2 σ detection. Hence we do not consider this source detected at 160 μm . The SPIRE detections may be spurious sources in the beam centered at the optical position of the source. However we cannot exclude the possibility that some of the SPIRE emission may be cold dust component whose peak emission is in the 250 μm band.

PG 1100+772 The 250 μm map for this source shows multiple faint sources in the central one arcminute region. It is thus possible that the 350 and 500 μm flux measurements are contaminated by emission from other sources. Given the poor angular resolution of the SPIRE 250 map and the fact that we do not detect additional sources in the higher resolution PACS data we cannot de-blend the 350 and 500 micron sources. Note however, that the centroid of the 250 μm emission is a full FWHM (18") away from the optical position of the source which does coincide with the PACS 70 μm emission centroid. As such we do not include the SPIRE points in our analysis and instead use our measurements as upper limits.

PG1114+445 The peak of the SPIRE flux derived from the time line is only 7" away from the centroid of the 70 μm emission. However the SPIRE 250 μm map shows emission 39" away from the PACS 70 μm centroid, while the 350 μm map shows emission 20" away from the PACS 70 μm centroid and at the same position angle as the 250 μm emission. Therefore we cannot rule out that the SPIRE photometry is contaminated by a spurious source. If the spurious source is at the same redshift as PG 1114+445, they would be 300 kpc apart. We set the values we measure at 350 and 500 μm as upper limits.

PG1119+120 The 70 μm field includes four other source less than 1' from PG 1119+120's optical position. The 160 μm flux measurement is more susceptible than those at 70 and 100 μm to contamination from those sources due to the larger PSF at 160 μm which can be seen in the larger error bar.

PG 1211+143 The 350 and 500 μm maps show some faint structure, and spurious sources close to the position of PG 1211+143 may have artificially increased the flux by around 20-30% at those wavelengths based on the ratio of the faint likely spurious emission around the source and the source.

PG 1302-102 The 250, 350 and 500 μm measurements are very secure as the central source in each of the maps is bright and compact. The increasing flux with wavelength, although unusual, appears to be real, and may be related to the significant contribution of non-thermal continuum.

PG1309+355 Both, our PACS 70 μm estimate matches the *Spitzer* MIPS 70 μm measurement (Shang et al. 2011), and our estimate at 160 μm are $59 \pm 21 \text{ mJy}$ matches those from *Spitzer* MIPS at 160 μm : $46 \pm 12 \text{ mJy}$. We note the presence of a spurious source in the PACS 160 μm map 80" away from PG1309+355.

PG1322+659 At all PACS wavelengths this source is composed of two overlapping blobs (one significantly brighter than the second) the same size as our PSF, with the centroid of the combined emission within 2" of the optical position. The photometry we report here corresponds to the combined fluxes from those blobs. We also note the presence of an extended system composed of a faint ring about 17" in size, with a central unresolved blob, located at an angular distance of 35" from the optical position of PG1322+659 source in the 70 μm map.

PG 1341+258 An extended (20-30") source at the edge of the image may impact the flux measured for this source because it increases the background throughout the image given the large PACS PSF¹³. This affects the 160 μm data because of its worst angular resolution among the PACS observations.

At 500 μm we find spurious emission from a source that is 1' away from the PACS 70 μm emission centroid. We use the measured emission to estimate upper limits at 500 μm .

PG 1354+213 The SPIRE source we detect in the vicinity of our source ($\sim 13''$ away from the 70 μm emission centroid) does not appear to be associated with PG 1354+213 both because of their positions and also because they are a factor of a few brighter than the emission at 160 μm . We use our time-line data measurement to determine an upper limit for the SPIRE emission associated with the QSO.

¹² The diameter of the region that would include 80% of a point source energy is 100" at 100 μm (Gillett, F. et al. 1985, Ch. II IRAS Catalogs and Explanatory Supplement, U.S. Government Printing Office)

¹³ Only 90% of the total energy of a source is included in the inner 20-30" distance from a source. Please refer to: http://herschel.esac.esa.int/twiki/pub/Public/PacsCalibrationWeb/PhotMiniScan_ReleaseNote_20101112.pdf

PG 1612+261 The 500 μm measurement from the time-line is higher than what would be expected from the modified black-body that fits the PACS measurements as well as the 250 and 350 μm data points (see section 3.4). Since the SPIRE 500 μm map does not show a conclusive detection we use the time-line estimate as an upper-limit, but cannot rule out that this source has a cold dust emission component in excess of what can be determined from a modified black-body fit to the 70-350 μm measurements.

PG 1704+608 The 250 and 350 μm emission centroids are within a PSF away from 70 μm emission centroid, however the 500 μm emission center is $\sim 36''$ away, i.e. about 1 FWHM. For reference that source at 500 μm is 33 ± 9 mJy and we use this measurement to derive an upper limit at 500 μm .

PG 2209+184 The 500 μm point from the time-line fits is higher than what would be expected from the modified black-body that fits the PACS measurements as well as the 250 and 350 μm data points (see section 3.4). In the 250 and 350 μm maps we see 3 sources within $80''$ of the position of the source, note that is more than the PSF width at 500 μm of $\sim 37''$. Therefore we cannot conclusively determine whether the high value of the estimated flux at 500 μm is due to contamination from the sources around it or an excess of cold dust in the host galaxy.

PG 2304+042 The SPIRE maps are dominated by several sources as well as faint extended emission around the central area, perhaps associated with a foreground object. The morphologies of the SPIRE detections do not match the morphology of the faint 70 μm emission. The timeline fitting at the optical position of PG2304+042 results in detections at 250 and 350 μm which we present in Table 3. However the SPIRE emission we measure may be spurious and not physically associated with the source, but we do present them as detections as they are located at the correct optical position and are above 3σ .

A2: SYNCHROTRON VERSUS THERMAL DUST EMISSION

We investigate the radio properties of the PG QSOs to estimate the amount of synchrotron radiation which contributes to the observed FIR emission in radio loud PG QSOs.

We compile observations of PG QSOs at 1.4 GHz from the Faint Images of the Radio Sky at Twenty-cm (Becker et al. 1995, FIRST), the NRAO Very Large Array Survey (Condon et al. 1998, NVSS), and 5 GHz VLA data from (Kellermann et al. 1989). The FIRST survey covered 10,000 square degrees with a 1.0 mJy source detection threshold and a spatial resolution of $5''$. NVSS covers the entire sky north of -40 deg declination to a completeness limit of 2.5 mJy and a spatial resolution of $45''$. The observations of Kellermann et al. (1989) used to estimate total fluxes at 5 GHz reached a sensitivity of 0.065 mJy and a spatial resolution of $18''$. Note that Kellermann et al. (1989) observed a subset of the PG QSOs at a higher resolution of $0.5''$ to determine the strength of unresolved components. Here we only use the $18''$ resolution data.

Two definitions are used to demarcate radio-quiet and radio loud QSOs. One criterion is based on the ratio of optical to radio flux R . As defined and measured by (Kellermann et al. 1989), R is the ratio of the total flux density at 6 cm to the optical flux density at an effective wavelength of 4400 \AA . Using this definition and the R estimates from (Kellermann et al. 1989) 16 PG QSOs from our sample are radio loud. Peacock et al. (1986) point out that R can be used as a discriminating parameter only if the radio and optical luminosities are linearly correlated, which is not the case (Stocke et al. 1992). Note however, that on the basis of a radio-selected sample of 636 QSOs White et al. (2000) have argued that the distribution of radio characteristics is not bimodal.

The second definition (Gregg et al. 1996) divides sources at the 1.4 GHz luminosity of $3 \times 10^{25} \text{ W/Hz}$. Ivezić et al. (2002) found that the two definitions are consistent for optically selected QSOs. We compute the rest frame luminosities at 1.4 GHz assuming a spectral index of -0.5 (Stern et al. 2000) and find that $\sim 13\%$ are brighter at 1.4 GHz than 10^{25} W/Hz and would qualify as radio loud AGN under the definition of (Gregg et al. 1996).

We estimate the possible contributions of synchrotron emission at 250 μm using the example of Kalfountzou et al. (2014) using steeper spectral index of -0.7 . We find that only in 13 sources the contribution from synchrotron could exceed 10 mJy - the typical error on the measurements at 250 μm . However we note that only 7 of the PG QSOs have actually been detected at wavelengths longer than 250 μm .

To assess if and how our investigation of FIR properties of this sample of Type 1 QSOs is biased by the inclusion of radio loud QSOs we compare their FIR to their radio properties. Figure 12 shows $S_{250\mu\text{m}}/S_{24\mu\text{m}}$, $S_{350\mu\text{m}}/S_{250\mu\text{m}}$ and $L_{11.3\mu\text{mPAH}}/L_{\text{FIR}}$ as a function of the 1.4 GHz radio luminosity and the radio loudness factor R . We do not find any obvious trends between the IR slope and the radio luminosity, or R in agreement with the work of (Kalfountzou et al. 2014) and so our results in the FIR do not appear biased by the radio loud sources in the sample.

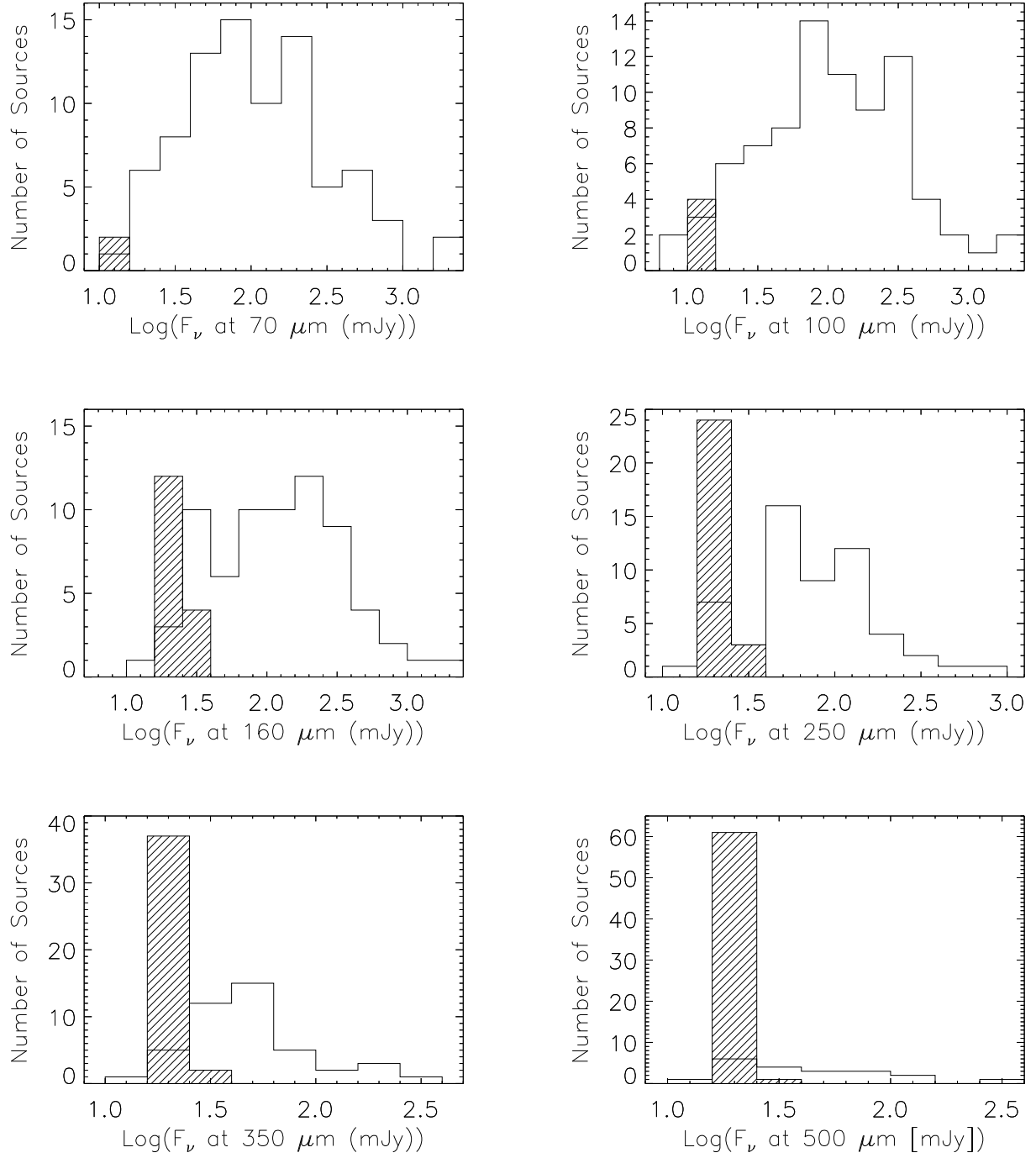


Figure 1. Histograms observed Herschel PACS and SPIRE fluxes at 70, 100, 160, 250, 350, and 500 μm . The upper limits are shown as dashed histograms.

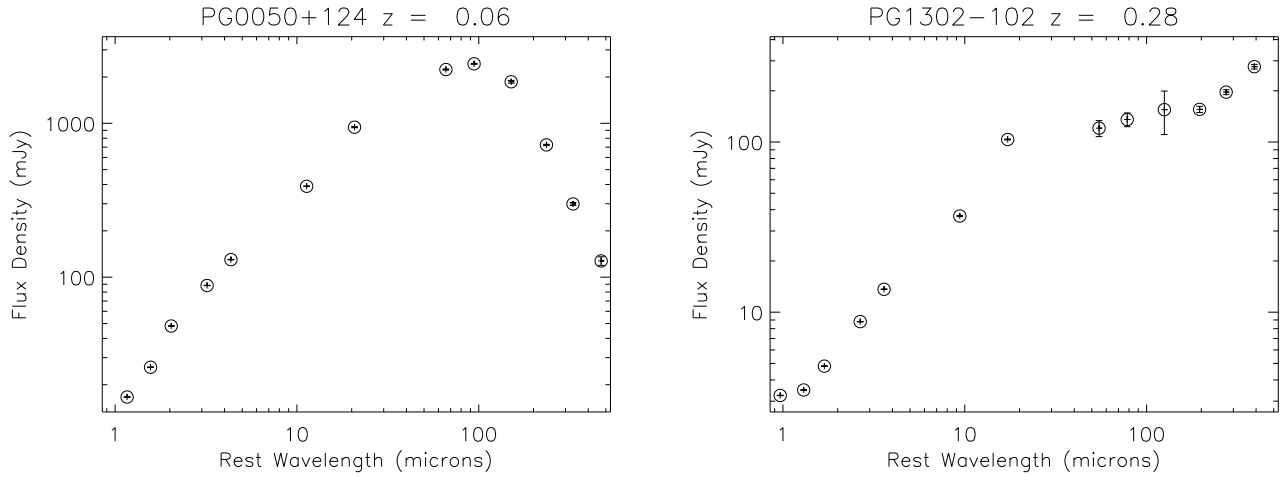


Figure 2. NIR to FIR SEDs of PG 0050+124 and radio loud source PG 1302-102. All the SEDs are available in the electronic version of this paper.

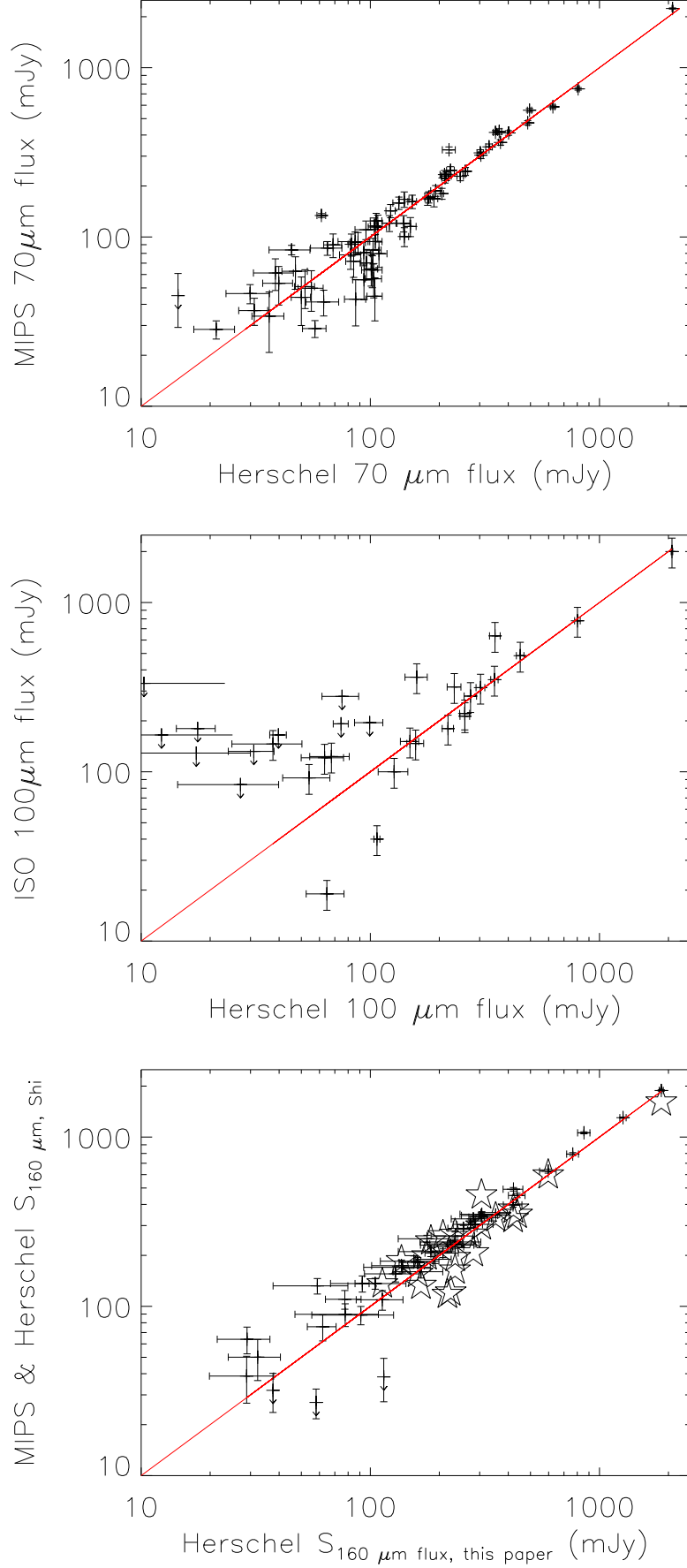


Figure 3. Herschel measurements at 70, 100 and 160 μ m presented in this paper versus MIPS 70 μ m measurements from Shi et al. (2014), ISO 100 μ m data from ISO Haas et al. (2003) and MIPS (stars) and Herschel (crosses) measurements from Shi et al. (2014)

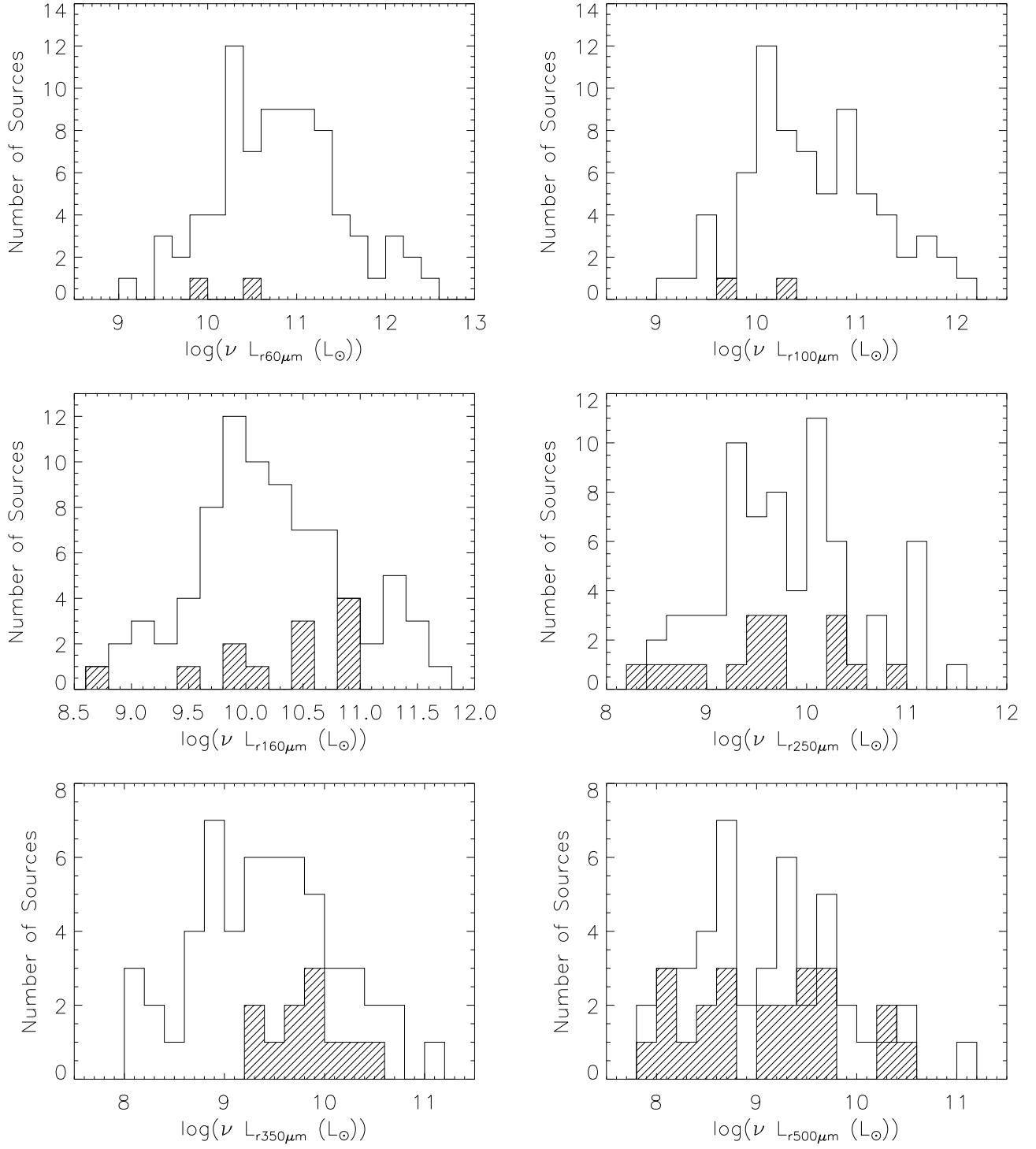


Figure 4. Histograms of rest-frame luminosities at 60-500 μm obtained from *Herschel* photometric measurements. The upper limits are shown as dashed histograms.

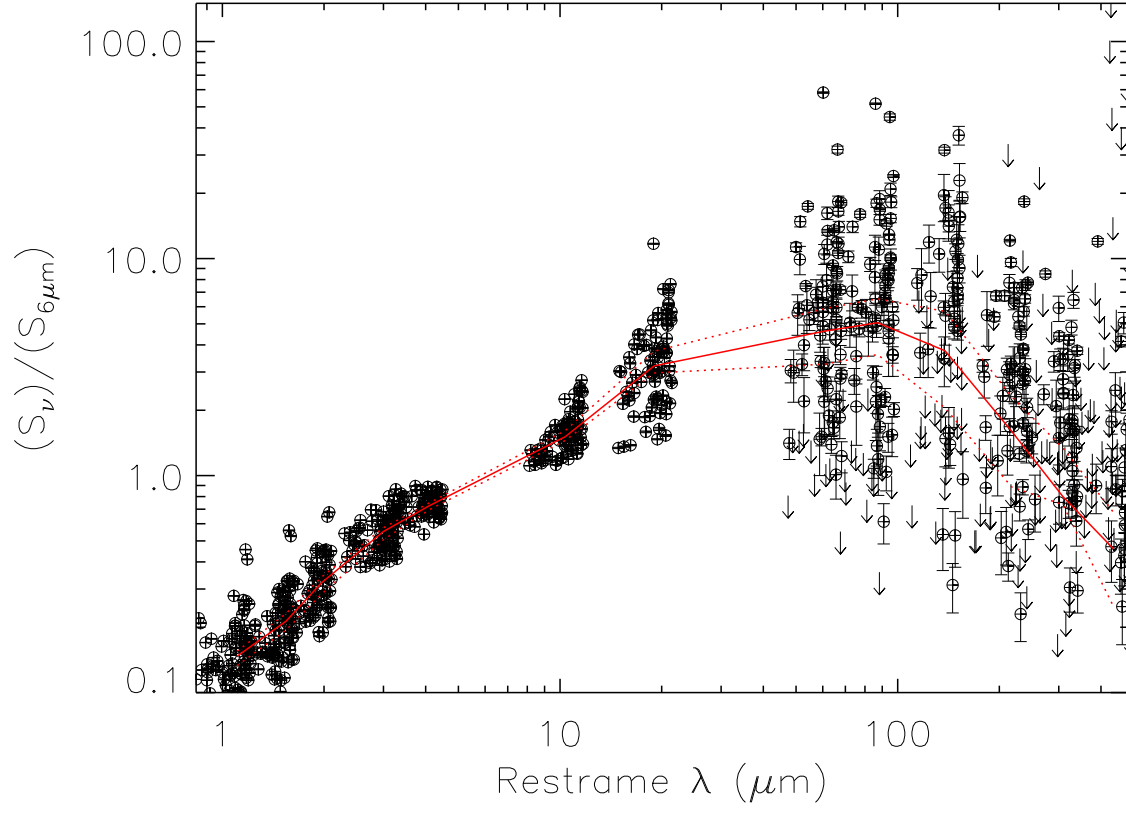


Figure 5. The combined photometry of all the 85 sources in our sample normalized by the estimated luminosity at $6\ \mu\text{m}$. Top: solid line gives the median template computed in each observed photometric band using the Kaplan-Meier estimator, the dotted lines show the 95% confidence interval.

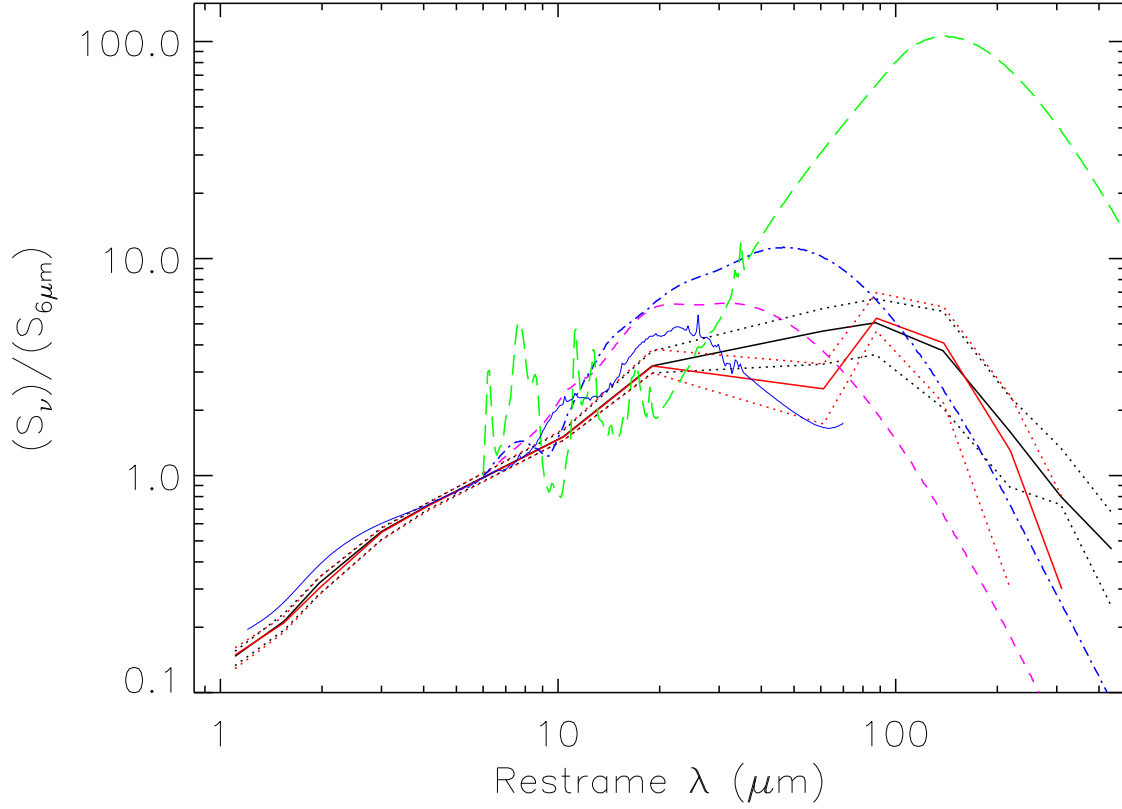


Figure 6. Comparison of median SEDs derived from (1) the entire PG QSOs sample presented in this paper (black lines), (2) only the radio quiet sources (red lines), (3) starburst template from Mullaney et al. (2011), (4) average observed SED of 28 PG QSOs observed with IRS from Netzer et al. (2007) (magenta solid), (5) average intrinsic AGN SED of 8 ‘FIR-weak’ PG QSOs, after subtraction of a starburst component from Netzer et al. (2007) (blue solid), (6) average high-luminosity: $\log(L_{2-10\text{keV}} \geq 42.9)$, nearby AGN template (dashed magenta) from Mullaney et al. (2011), and (7) average low-luminosity: $\log(L_{2-10\text{keV}} \geq 42.9)$, nearby AGN template (dot-dash blue line) from Mullaney et al. (2011). See Fig. 5 for photometry of individual PG QSOs normalized at $6\text{ }\mu\text{m}$.

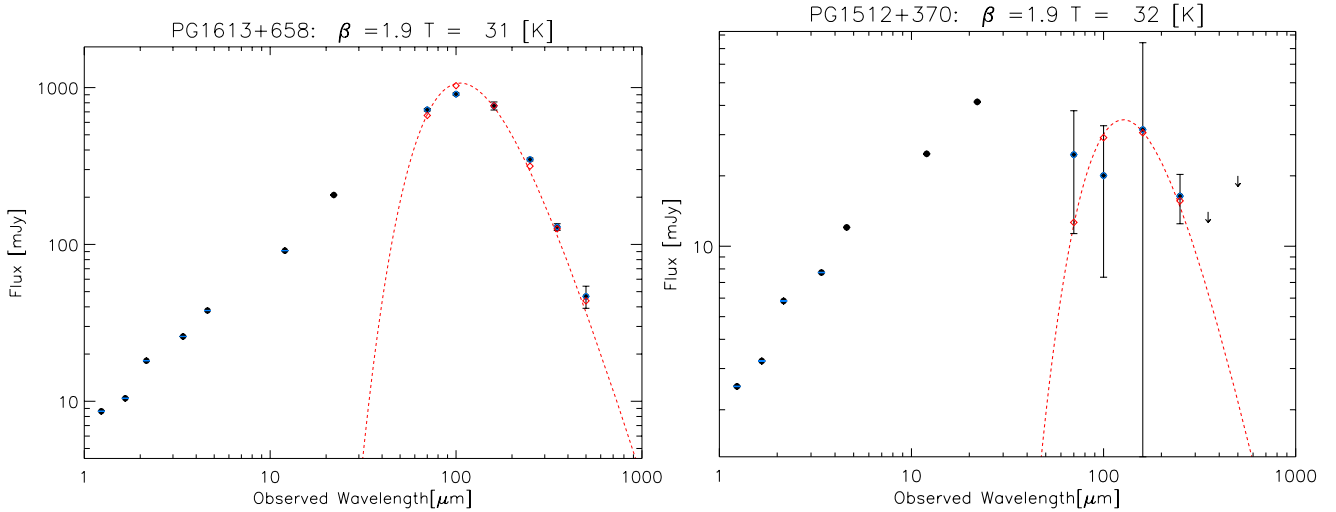


Figure 7. Examples of good and poor fits. Less than 10% of the sources have such poor fits, and those are poor because of low signal to noise ratios on individual measurements.

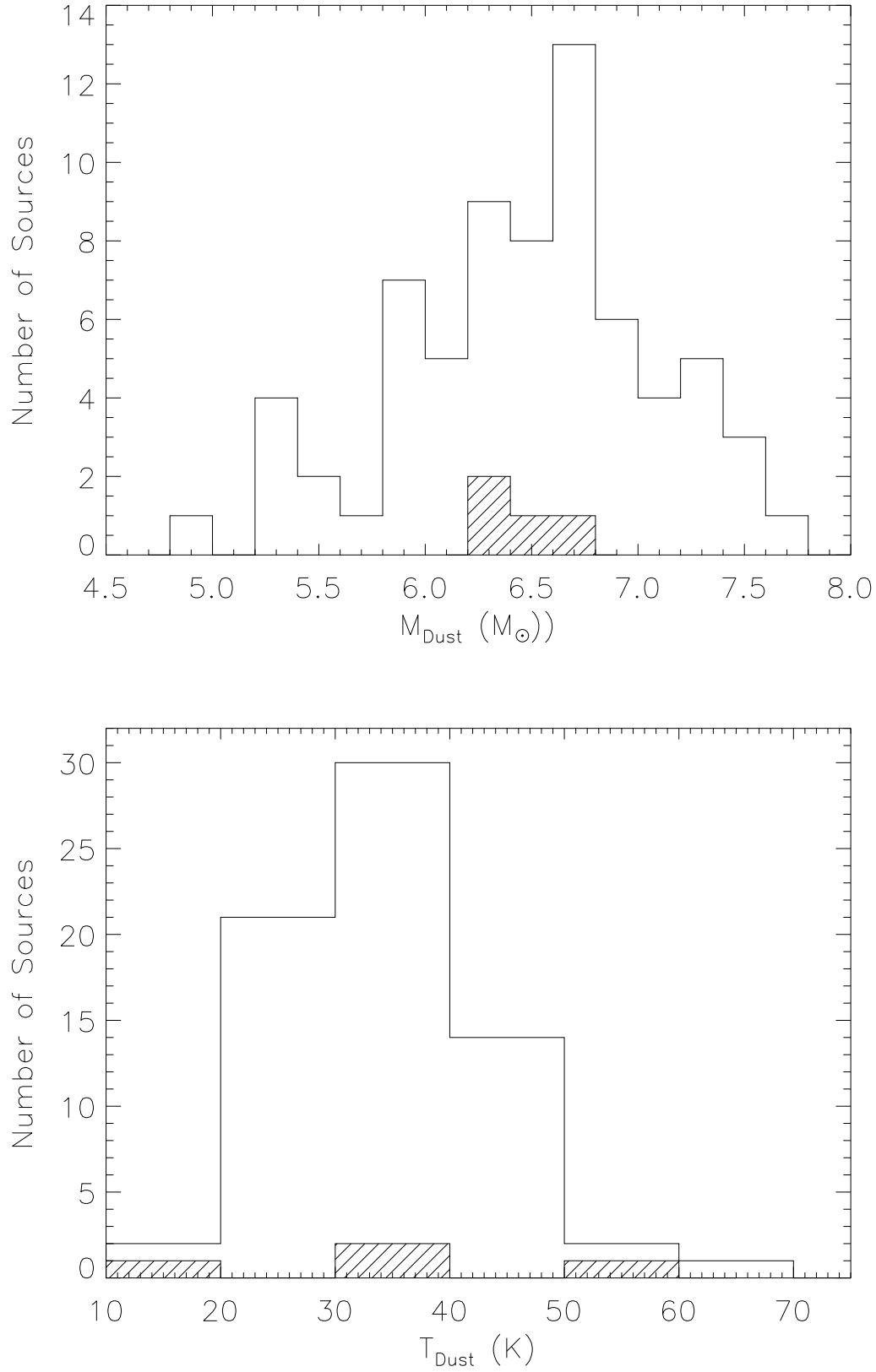


Figure 8. Histogram of dust masses, temperatures estimated from single temperature modified black-body fits with an emissivity spectral index β of 1.91 (see section 3.4). The dashed histograms shows the result of poor fits with only 2 or 3 photometric points, or 4 points with large errors.

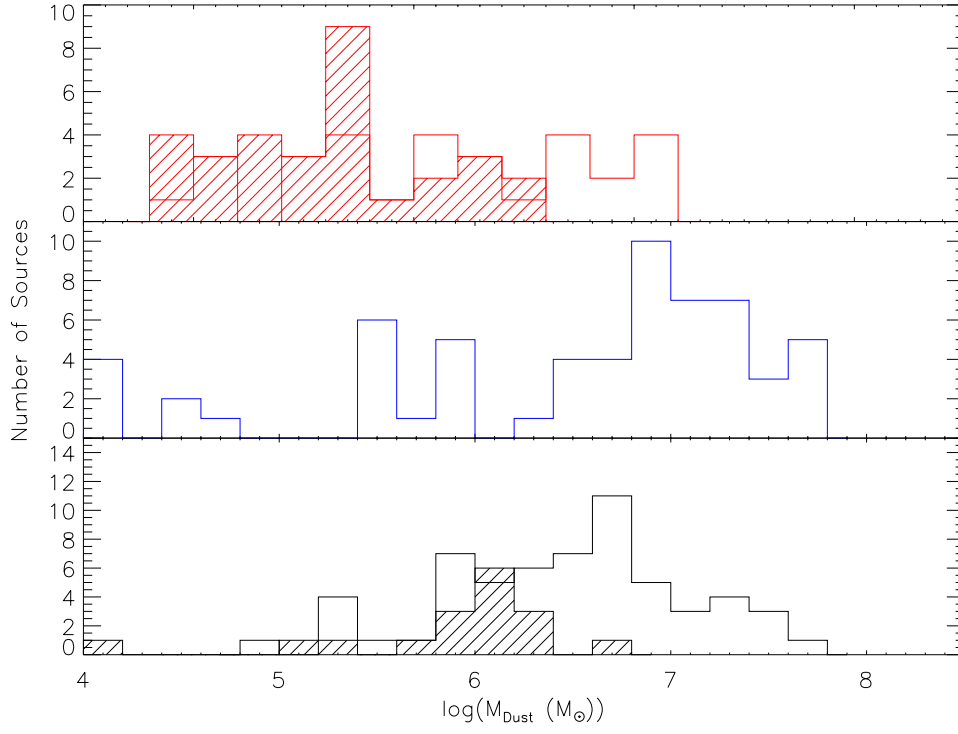


Figure 9. Histograms of dust masses in massive elliptical galaxies (top red), nearby spirals (middle blue) and the PG QSOs presented in this paper (bottom black).

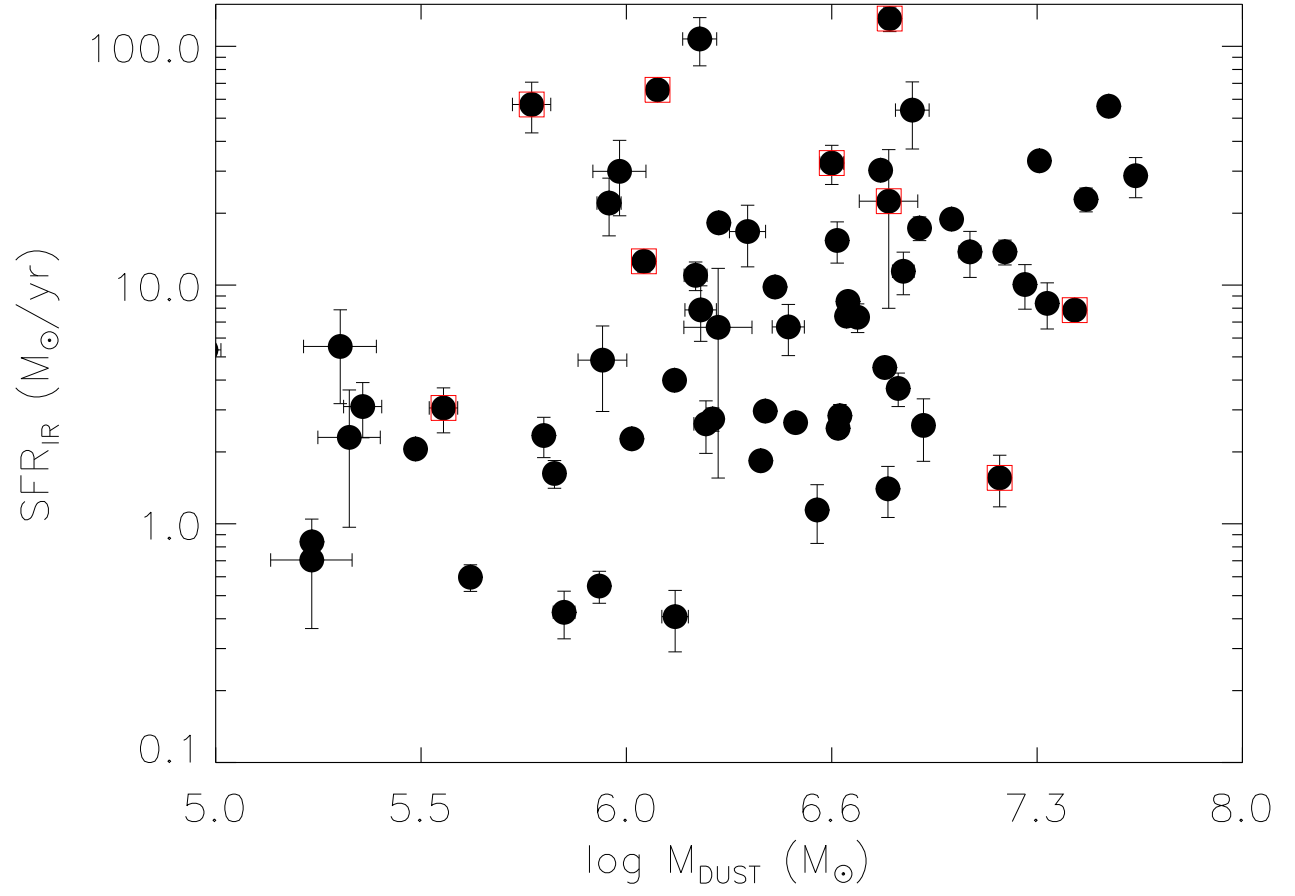


Figure 10. Star-formation rates derived from the FIR using the relation of (Murphy et al. 2011) versus total dust masses estimated from the single temperature modified black body fits. Red squares represent radio-loud sources, using the (Kellermann et al. 1989) definition of radio-loud quasars.

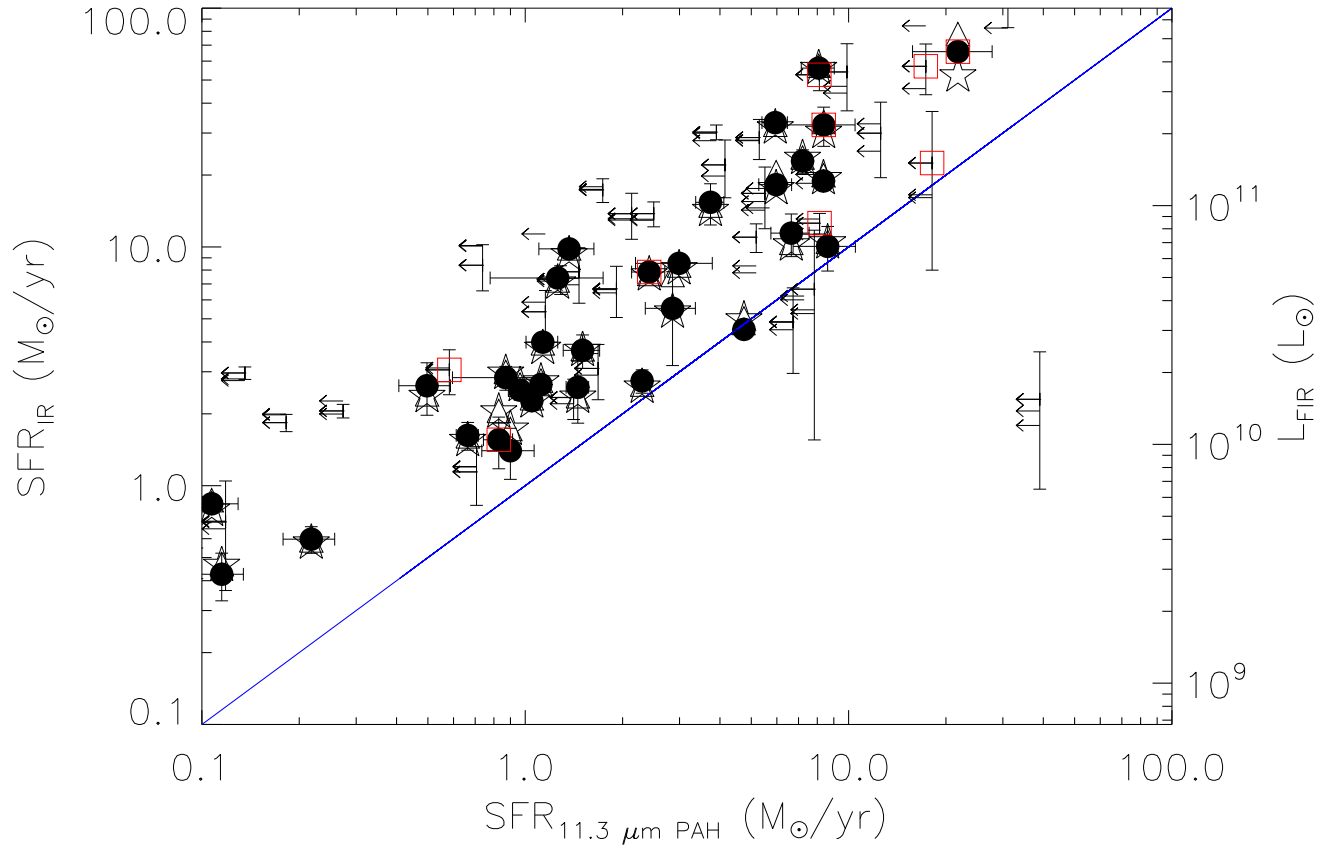


Figure 11. Star-formation rates derived from the PAH $11.3 \mu\text{m}$ measurements of (Shi et al. 2007) versus the total FIR luminosities, and the SFR derived from the FIR using the relation of (Murphy et al. 2011). Solid circles are SFR rates estimated from the 42.5 to $122.5 \mu\text{m}$ FIR as defined by Helou et al. (1985), the stars and triangles are SFR rates estimated from the 40 - $500 \mu\text{m}$ and the 8 - $1000 \mu\text{m}$ respectively, as computed from the single temperature modified black body fits. Red squares mark radio-loud sources, using the (Kellermann et al. 1989) demarcation of radio-loud quasars.

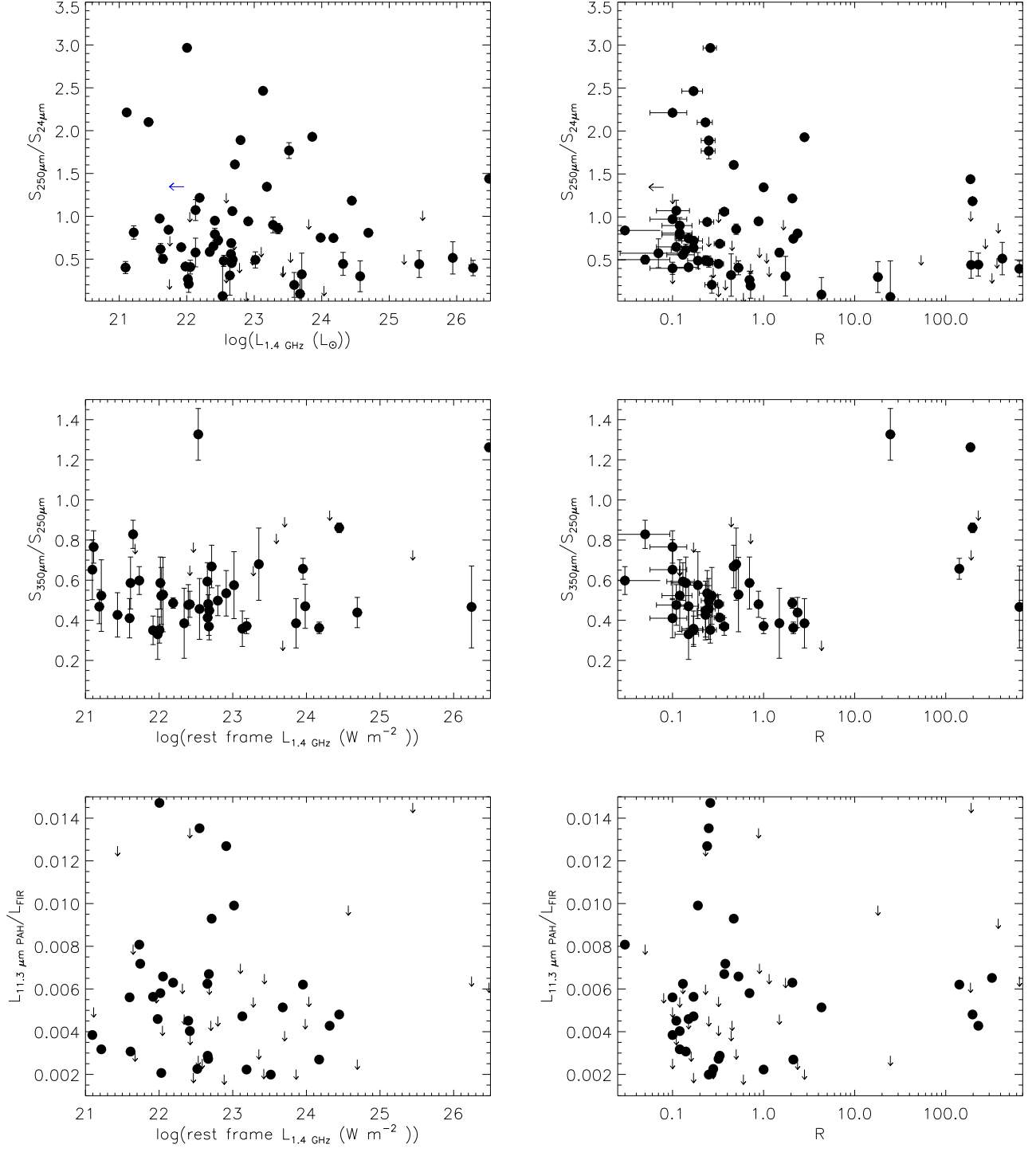


Figure 12. \log (Radio Luminosity (W/Hz)) (left) and ratio of radio to optical luminosity (R) versus (right) versus: (top) the ratio of $250 \mu\text{m}$ rest-frame Luminosity to the $24 \mu\text{m}$ rest-frame luminosity, (middle) the ratio of $350 \mu\text{m}$ rest-frame Luminosity to the $250 \mu\text{m}$ rest-frame luminosity, (bottom) the ratio of $11.3 \mu\text{m}$ PAH luminosity to the FIR luminosity.

REFERENCES

- Armus, L., Charmandaris, V., Bernard-Salas, J., et al. 2007, *ApJ*, 656, 148
- Bechtold, J., Czerny, B., Elvis, M., Fabbiano, G., & Green, R. F. 1987, *ApJ*, 314, 699
- Becker, R. H., White, R. L., & Helfand, D. J. 1995, *ApJ*, 450, 559
- Bendo, G. J., Griffin, M. J., Bock, J. J., et al. 2013, *MNRAS*, 433, 3062
- Bertram, T., Eckart, A., Fischer, S., et al. 2007, *A&A*, 470, 571
- Bianchi, S. 2013, *A&A*, 552, A89
- Boroson, T. A. 2002, *ApJ*, 565, 78
- Boroson, T. A., & Green, R. F. 1992, *ApJS*, 80, 109
- Boyle, B. J. 1990, *MNRAS*, 243, 231
- Brotherton, M. S., Tran, H. D., Becker, R. H., et al. 2001, *ApJ*, 546, 775
- Compiègne, M., Flagey, N., Noriega-Crespo, A., et al. 2010, *ApJ*, 724, L44
- Compiègne, M., Verstraete, L., Jones, A., et al. 2011, *A&A*, 525, A103
- Condon, J. J. 1992, *ARA&A*, 30, 575
- Condon, J. J., Cotton, W. D., Greisen, E. W., et al. 1998, *AJ*, 115, 1693
- Cristiani, S., & Vio, R. 1990, *A&A*, 227, 385
- Dasyra, K. M., Tacconi, L. J., Davies, R. I., et al. 2007, *ApJ*, 657, 102
- Diamond-Stanic, A. M., & Rieke, G. H. 2010, *ApJ*, 724, 140
- Díaz-Santos, T., Alonso-Herrero, A., Colina, L., et al. 2010, *ApJ*, 711, 328
- Draine, B. T., & Li, A. 2007, *ApJ*, 657, 810
- Draine, B. T., Dale, D. A., Bendo, G., et al. 2007, *ApJ*, 663, 866
- Elvis, M., Green, R. F., Bechtold, J., et al. 1986, *ApJ*, 310, 291
- Elvis, M., Wilkes, B. J., McDowell, J. C., et al. 1994, *ApJS*, 95, 1
- Esquej, P., Alonso-Herrero, A., González-Martín, O., et al. 2014, *ApJ*, 780, 86
- Evans, A. S., Frayer, D. T., Surace, J. A., & Sanders, D. B. 2001, *AJ*, 121, 1893
- Feigelson, E. D., & Jogesh Babu, G. 2012, *Modern Statistical Methods for Astronomy* (Cambridge University Press)
- Ferrarese, L., & Merritt, D. 2000, *ApJ*, 539, L9
- Francis, P. J., Hewett, P. C., Foltz, C. B., et al. 1991, *ApJ*, 373, 465
- Gebhardt, K., Kormendy, J., Ho, L. C., et al. 2000, *ApJ*, 543, L5
- Glikman, E., Helfand, D. J., & White, R. L. 2006, *ApJ*, 640, 579
- Gregg, M. D., Becker, R. H., White, R. L., et al. 1996, *AJ*, 112, 407
- Griffin, M. J., Abergel, A., Abreu, A., et al. 2010, *A&A*, 518, L3
- Guyon, O., Sanders, D. B., & Stockton, A. 2006, *ApJS*, 166, 89
- Haas, M., Klaas, U., Müller, S. A. H., et al. 2003, *A&A*, 402, 87
- Hanish, D. J., Teplitz, H. I., Capak, P., et al. 2013, *ApJ*, 768, 13
- Helou, G., Soifer, B. T., & Rowan-Robinson, M. 1985, *ApJ*, 298, L7
- Ho, L. C., Darling, J., & Greene, J. E. 2008, *ApJ*, 681, 128
- Inami, H., Armus, L., Surace, J. A., et al. 2010, *AJ*, 140, 63
- Ivezić, Ž., Menou, K., Knapp, G. R., et al. 2002, *AJ*, 124, 2364
- Kalfountzou, E., Stevens, J. A., Jarvis, M. J., et al. 2014, *MNRAS*, 442, 1181
- Kellermann, K. I., Sramek, R., Schmidt, M., Shaffer, D. B., & Green, R. 1989, *AJ*, 98, 1195
- Kennicutt, R. C., & Evans, N. J. 2012, *ARA&A*, 50, 531
- Kormendy, J., & Ho, L. C. 2013, *ARA&A*, 51, 511
- LaMassa, S. M., Heckman, T. M., Ptak, A., et al. 2012, *ApJ*, 758, 1
- Lutz, D. 2014, *ARA&A*, 52, 373
- Magorrian, J., Tremaine, S., Richstone, D., et al. 1998, *AJ*, 115, 2285
- Marshall, J. A., Herter, T. L., Armus, L., et al. 2007, *ApJ*, 670, 129
- Mullaney, J. R., Alexander, D. M., Goulding, A. D., & Hickox, R. C. 2011, *MNRAS*, 414, 1082
- Murphy, E. J., Condon, J. J., Schinnerer, E., et al. 2011, *ApJ*, 737, 67
- Netzer, H., Lutz, D., Schweitzer, M., et al. 2007, *ApJ*, 666, 806
- Neugebauer, G., Miley, G. K., Soifer, B. T., & Clegg, P. E. 1986, *ApJ*, 308, 815
- Nguyen, H. T., Schulz, B., Levenson, L., et al. 2010, *A&A*, 518, L5
- Peacock, J. A., Miller, L., & Longair, M. S. 1986, *MNRAS*, 218, 265
- Pearson, C., Lim, T., North, C., et al. 2013, *Experimental Astronomy*, arXiv:1401.2036
- Petric, A. O., Armus, L., Howell, J., et al. 2011, *ApJ*, 730, 28
- Pilbratt, G. L., Riedinger, J. R., Passvogel, T., et al. 2010, *A&A*, 518, L1
- Poglitsch, A., Waelkens, C., Geis, N., et al. 2010, *A&A*, 518, L2
- Roche, P. F., Aitken, D. K., Smith, C. H., & Ward, M. J. 1991, *MNRAS*, 248, 606
- Sanders, D. B., Soifer, B. T., Elias, J. H., et al. 1988a, *ApJ*, 325, 74
- Sanders, D. B., Soifer, B. T., Elias, J. H., Neugebauer, G., & Matthews, K. 1988b, *ApJ*, 328, L35
- Schmidt, M., & Green, R. F. 1983, *ApJ*, 269, 352
- Scott, J. E., Kriss, G. A., Brotherton, M., et al. 2004, *ApJ*, 615, 135
- Scoville, N. Z., Frayer, D. T., Schinnerer, E., & Christopher, M. 2003, *ApJ*, 585, L105
- Serjeant, S., & Hatziminaoglou, E. 2009, *MNRAS*, 397, 265
- Shang, Z., Brotherton, M. S., Wills, B. J., et al. 2011, *ApJS*, 196, 2
- Shi, Y., Rieke, G. H., Ogle, P. M., Su, K. Y. L., & Balog, Z. 2014, *ApJS*, 214, 23
- Shi, Y., Ogle, P., Rieke, G. H., et al. 2007, *ApJ*, 669, 841
- Skibba, R. A., Engelbracht, C. W., Dale, D., et al. 2011, *ApJ*, 738, 89
- Skrutskie, M. F., Cutri, R. M., Stiening, R., et al. 2006, *AJ*, 131, 1163
- Smith, M. W. L., Gomez, H. L., Eales, S. A., et al. 2012, *ApJ*, 748, 123
- Stern, D., Djorgovski, S. G., Perley, R. A., de Carvalho, R. R., & Wall, J. V. 2000, *AJ*, 119, 1526
- Stocke, J. T., Morris, S. L., Weymann, R. J., & Foltz, C. B. 1992, *ApJ*, 396, 487
- Telfer, R. C., Zheng, W., Kriss, G. A., & Davidsen, A. F. 2002, *ApJ*, 565, 773
- Tremaine, S., Gebhardt, K., Bender, R., et al. 2002, *ApJ*, 574, 740
- Vanden Berk, D. E., Richards, G. T., Bauer, A., et al. 2001, *AJ*, 122, 549
- Veilleux, S., Kim, D.-C., Rupke, D. S. N., et al. 2009, *ApJ*, 701, 587
- White, R. L., Becker, R. H., Gregg, M. D., et al. 2000, *ApJS*, 126, 133
- Wright, E. L., Eisenhardt, P. R. M., Mainzer, A. K., et al. 2010, *AJ*, 140, 1868
- Zheng, W., Kriss, G. A., Telfer, R. C., Grimes, J. P., & Davidsen, A. F. 1997, *ApJ*, 475, 469

Table 1
FIR Fluxes from PACS and SPIRE photometry

Name	F _{70μm} [mJy]	σ _{70μm} [mJy]	F _{100μm} [mJy]	σ _{100μm} [mJy]	F _{160μm} [mJy]	σ _{160μm} [mJy]	F _{250μm} [mJy]	σ _{250μm} [mJy]	F _{350μm} [mJy]	σ _{350μm} [mJy]	F _{500μm} [mJy]	σ _{500μm} [mJy]
PG 0003+158	28	4	23	13.	< 24	...	< 30	...	< 25	...	< 24	...
PG 0003+199	341	13	235	17	112	38	66	7	34	7.	< 23	...
PG 0007+106	234	13	258	13	235	51	181	7	156	6.	154	9.
PG 0026+129	24	14	25	8.	< 25	...	< 25.	...	< 22	...	< 21	...
PG 0043+039	61	13	55	13	78	31	31	6.	< 23	...	< 22	...
PG 0049+171	45	16	39	13	32	18	< 23	...	< 26	...	< 23	...
PG 0050+124	2237	18	2436	17	1861	38	724	7	299	6	128	8
PG 0052+251	78	14	116	13	129	35	77	7	41	7	< 22	...
PG 0157+001	2334	19	2072	17	1267	40	486	6	176	7	71	9
PG 0804+761	143	13	63	13	32	8	< 23	...	< 22	...	< 23	...
PG 0838+770	167	18	218	12	217	39	106	6	50	6	< 22	...
PG 0844+349	65	14	134	16	234	69	84	5	50	5	31	7
PG 0921+525	110	14	142	12	81	40	63	5	24	6	< 22	...
PG 0923+129	808	20	1071	17	856	53	346	6	168	7	81	9
PG 0923+201	44	14	32	13.	< 23	...	16	5	< 23	...	< 22	...
PG 0934+013	229	14	262	17	287	57	< 26	...	< 21	...	< 24	...
PG 0947+396	114	20	172	13	192	34	123	7	61	7	< 22	...
PG 0953+414	28	13	21	12	17	7	14	4	< 21	...	< 24	...
PG 1001+054	53	14	38	13	17	12	< 22	...	< 24	...	< 23	...
PG 1004+130	116	13	117	17	44	38	40	8	< 21	...	< 21	...
PG 1011-040	172	13	246	13	234	53	115	6	47	6	< 24	...
PG 1012+008	81	13	88	13	78	37	56	7	38	12	< 23	...
PG 1022+519	228	14	296	17	255	37	123	7	53	8	< 23	...
PG 1048+342	41	7	96	13	166	41	65	6	50	7	< 23	...
PG 1048-090	29	3	24	3.	< 18	...	< 23	...	< 22	...	< 23	...
PG 1049-005	244	13	230	14	138	45	90	26	56	21	< 22	...
PG 1100+772	134	4	107	3	109	72	< 24	...	< 22	...	< 22	...
PG 1103-006	50	13	16	14.	< 25	...	< 23	...	< 22	...	< 23	...
PG 1114+445	93	13	66	14	52	46	< 25	...	< 21	...	< 22	...
PG 1115+407	168	18	288	13	274	35	153	7	55	6	< 24	...
PG 1116+215	86	15	62	6	30	10	22	8	< 24	...	< 22	...
PG 1119+120	414	11	394	12	352	51	107	5	35	6	< 23	...
PG 1121+422	< 15	...	< 15	...	< 23	...	< 23.	...	< 22	58.	< 23	...
PG 1126-041	561	14	582	14	437	36	193	7	68	6	38	8
PG 1149-110	327	13	303	13	306	60	129	6	62	6	32	6
PG 1151+117	34	13	11	12.	< 23	...	< 23	...	< 24	...	< 24	...
PG 1202+281	94	13	88	13	68	31	43	7	25	6	18	4
PG 1211+143	120	13	75	14	38	11	17	4	22	5	18	6
PG 1216+069	23	13	17	13.	< 23	...	< 23	...	< 22	...	< 22.	...
PG 1229+204	162	15	232	16	177	44	103.	6.	49	7	< 24	...
PG 1244+026	187	14	159	18	101	89	49	6	26	7	< 22	...
PG 1259+593	14	15	9	13.	< 24	...	< 23	...	< 22	...	< 22	...
PG 1307+085	43	13	50	12	29	8	< 23	...	< 23	...	< 21	...
PG 1309+355	84	5	74	6	59	21	33	7	12	6	< 23	...
PG 1310-108	94	10	93	19	82	108	54	6	35	9	< 23	...
PG 1322+659	115	15	127	19	92	6	45	6	< 21	...	< 21	...
PG 1341+258	84	14	88	16	62	9	41	7	21	5	< 22	...
PG 1351+236	362	13	511	17	421	42	208	6	73	6	15	...
PG 1351+640	587	13	529	12	306	37	45	6	< 25	...	< 23	...
PG 1352+183	24	13	18	3	15	8	< 25	...	< 22	...	< 22	...
PG 1354+213	51	13	40	3	32	8	< 25	...	< 23	...	< 22	...
PG 1402+261	247	13	259	13	137	35	66	6	30	6	19	6
PG 1404+226	63	14	68	13	77	14	57	6	38	6	< 25	...
PG 1411+442	101	13	131	13	116	57	72	6	42	6	23	6
PG 1415+451	124	14	158	13	90	65	61	6	< 22	...	< 24	...
PG 1416-129	46	6	31	7	29	9	< 26	...	< 22	...	< 24	..
PG 1425+267	91	13	65	12	17	44	< 24	...	< 22	...	< 25	8.
PG 1426+015	314	13	348	13	305	55	< 26	...	< 27	...	< 22	...
PG 1427+480	80	14	54	13	44	32	27	6	< 21	...	< 23	...
PG 1435-067	31	14	< 13	...	< 25	...	25	7	< 22	...	< 23	...
PG 1440+356	750	13	802	23	597	50	248	6	92	5	47	6
PG 1448+273	159	13	175	13	161	27	58	6	27	6	< 23	...
PG 1501+106	420	16	350	19	270	115	< 25	...	< 26	...	< 23	...
PG 1512+370	30	13	27	13	32	26	16	4	< 25	...	< 23	...
PG 1519+226	72	14	99	14	91	35	< 25	...	< 23	...	< 24	...
PG 1534+580	168	14	188	18	217	130	50	6	29	6	< 22	...
PG 1535+547	70	14	59	12	60	34	50	6	29	6	< 22	...
PG 1543+489	304	14	274	17	208	34	86	6	41	7	< 22	...
PG 1545+210	20	13	< 12	...	< 22	...	17	5	< 22	...	< 23	...
PG 1552+085	37	4	44	3	27	5	< 24	...	< 23	...	< 22	...
PG 1612+261	223	15	258	24	224	59	86	...	33	5	< 23	...
PG 1613+658	722	12	909	16	765	45	348	7	129	6	47	8
PG 1617+175	34	14	34	14.	< 25	42	< 23	...	< 24	...	< 24	...

Table 1 — *Continued*

Name	$F_{70\mu m}$ [mJy]	$\sigma_{70\mu m}$ [mJy]	$F_{100\mu m}$ [mJy]	$\sigma_{100\mu m}$ [mJy]	$F_{160\mu m}$ [mJy]	$\sigma_{160\mu m}$ [mJy]	$F_{250\mu m}$ [mJy]	$\sigma_{250\mu m}$ [mJy]	$F_{350\mu m}$ [mJy]	$\sigma_{350\mu m}$ [mJy]	$F_{500\mu m}$ [mJy]	$\sigma_{500\mu m}$ [mJy]
PG 1626+554	< 13	...	< 13	...	< 25	...	23	7	38	6	33	7
PG 1700+518	411	13	378	12	282	56	128	6	56	6	21	5
PG 1704+608	180	13	149	14	113	26	51	7	24	7	< 22	...
PG 2112+059	90	14	79	13	88	40	< 26	...	< 22	...	< 23	...
PG 2130+099	472	14	451	17	420	39	158	6	76	5.	42	7
PG 2209+184	64	14	121	14	184	51	110	6	72	6.	76	9
PG 2214+139	57	13	85	13	105	38	50	4	41	5.	24	7
PG 2233+134	56	13	50	13	33	21	< 23	...	< 22	...	< 22	...
PG 2251+113	45	13	42	14.	< 23	...	< 25	...	< 23	...	< 22	...
PG 2304+042	23	12	9	8.	< 26	...	< 22	...	< 22	...	< 24	...
PG 2308+098	19	14	12	13.	< 24	...	< 23	...	< 24	...	< 24	...

Table 2
FIR Photometry Statistics

Data	Detection rate	Minimum [mJy]	Maximum [mJy]	Median [mJy]	Mean [mJy]	Standard Deviation	Median Error [mJy]	Median Upper Limit [mJy]
PACS 70 μ m	98%	14	2334	94	212	370	13	53
PACS 100 μ m	95%	9	2436	107	226	382	13	56
PACS 160 μ m	81%	15	1861	113	209	292	38	174
SPIRE 250 μ m	69%	14	724	63	104	121	6	59
SPIRE 350 μ m	55%	12	299	41	61	55	6	50
SPIRE 500 μ m	25%	15	277	34	58	63	7	55

Table 3
NIR, MIR, and Radio Fluxes

Name	z	J [mJy]	σ J [μ Jy]	H [mJy]	σ H [μ Jy]	Ks [mJy]	σ Ks [μ Jy]	F _{3.4μm} [mJy]	σ [μ Jy]	F _{4.6μm} [mJy]	σ [μ Jy]	F _{12μm} [mJy]	σ [μ Jy]	F _{22μm} [mJy]	σ [mJy]	L _{1.4GHz} Log [W/m ²]	Ref. ^a	R ^b
PG 0003+158	0.451	2.0	5	2.1	6	2.6	9	3.93	10	5.86	10	11.75	30	28	1	26.68	2	175.00
PG 0003+199	0.026	14.3	34	20.8	74	38.7	88	73.78	180	100.41	250	163.19	400	310	2	22.03	2	0.27
PG 0007+106	0.089	4.5	13	6.3	23	12.9	26	22.49	50	29.28	60	55.71	130	142	1	24.45	3	197.00
PG 0026+129	0.142	5.9	13	6.1	19	9.5	19	13.02	30	17.58	40	27.36	120	49	1	23.54	2	1.08
PG 0043+039	0.385	1.9	4	1.9	7	2.4	6	5.24	10	7.65	20	13.57	50	25	1	23.28	1	0.12
PG 0049+171	0.064	1.8	5	2.0	8	3.1	9	5.46	10	7.39	10	13.39	30	20	1	22.05	1	0.32
PG 0050+124	0.061	16.6	40	26.0	90	48.1	107	88.29	240	130.07	300	389.68	1140	944	8	22.66	3	0.33
PG 0052+251	0.155	4.4	10	5.5	13	8.5	15	11.97	20	16.83	40	37.32	80	83	1	22.91	1	0.24
PG 0157+001	0.163	3.8	12	6.0	16	10.4	23	15.49	30	21.49	40	90.34	210	469	3	24.17	3	2.12
PG 0804+761	0.100	10.3	17	15.0	27	28.7	55	64.49	160	87.62	220	134.62	340	217	1	22.88	2	0.60
PG 0838+770	0.131	1.5	7	2.0	11	3.6	14	7.57	20	9.61	20	26.30	50	75	1	21.19	1	0.11
PG 0844+349	0.064	6.9	14	7.9	18	10.4	21	16.81	40	22.05	50	48.25	110	106	1	21.73	1	0.03
PG 0921+525	0.035	4.5	16	5.6	24	8.4	25	24.01	50	31.43	70	64.43	150	108	1	22.34	3	1.49
PG 0923+129	0.029	11.4	28	14.5	56	20.1	46	22.99	50	30.16	60	108.72	260	254	2	22.19	3	2.07
PG 0923+201	0.192	2.9	7	4.5	13	8.8	20	20.68	40	25.62	60	35.67	80	56	1	22.64	1	1.74
PG 0934+013	0.050	1.6	10	2.1	12	2.6	13	5.94	10	8.08	20	30.75	70	87	1	21.74	1	0.38
PG 0947+396	0.206	2.0	5	2.7	7	5.2	11	8.10	20	13.06	30	26.47	60	55	1	22.80	1	0.25
PG 0953+414	0.234	3.3	7	4.1	8	6.5	13	18.82	40	24.18	50	30.25	70	50	1	23.70	1	0.44
PG 1001+054	0.160	1.5	5	2.2	6	3.8	10	9.49	20	13.56	30	23.50	60	39	1	22.97	1	0.50
PG 1004+130	0.241	3.4	8	3.5	11	4.9	13	8.17	20	12.02	20	35.41	90	82	1	24.32	3	228.00
PG 1011-040	0.058	3.5	15	4.3	24	5.8	21	10.45	20	13.46	30	44.45	110	112	1	21.60	1	0.10
PG 1012+008	0.187	1.7	9	2.2	12	3.9	16	8.46	20	12.24	30	29.37	80	62	1	23.35	3	0.50
PG 1022+519	0.045	3.1	9	4.2	15	5.5	15	11.21	20	12.91	30	26.54	60	49	1	21.43	3	0.23
PG 1048+342	0.167	1.3	4	1.5	5	2.4	8	4.05	10	5.88	10	13.52	30	27	1	21.11	1	0.10
PG 1048-090	0.344	0.9	3	1.3	5	1.8	7	5.05	10	7.08	10	10.33	30	24	1	26.62	1	377.00
PG 1049-005	0.360	2.1	5	2.8	9	4.8	13	9.14	20	13.58	30	18.69	40	23	1	23.52	1	0.25
PG 1100+772	0.311	2.6	6	2.7	9	4.0	11	8.46	20	12.85	20	23.29	50	52	1	26.79	2	322.00
PG 1103-006	0.423	2.1	5	2.8	9	4.8	13	9.14	20	13.58	30	18.69	40	23	1	26.67	1	272.00
PG 1114+445	0.144	3.4	7	4.0	9	7.8	13	13.89	30	22.79	50	60.02	130	148	1	22.32	1	0.13
PG 1115+407	0.155	2.2	8	3.1	13	5.2	15	9.31	20	11.82	20	23.92	50	49	1	23.13	3	0.17
PG 1116+215	0.176	5.8	12	8.6	18	16.1	28	35.77	80	48.77	100	69.23	180	117	1	23.59	3	0.72
PG 1119+120	0.050	6.0	19	7.4	25	9.6	27	16.67	40	24.83	50	98.24	230	243	1	21.98	3	0.15
PG 1121+422	0.225	1.4	4	1.9	8	3.3	7	5.09	10	7.10	10	9.68	20	13	1	21.69	1	0.10
PG 1126-041	0.062	8.6	28	13.6	45	22.8	59	35.70	80	47.40	110	116.49	290	276	2	21.92	1	0.17
PG 1149-110	0.049	5.2	24	6.1	37	8.5	32	12.35	30	13.94	30	40.84	100	121	1	22.42	1	0.88
PG 1151+117	0.177	1.8	5	2.1	9	3.9	13	4.85	10	7.59	10	15.41	40	31	1	21.47	1	0.07
PG 1202+281	0.165	2.0	5	2.5	7	4.7	10	7.73	20	10.85	20	28.57	60	86	1	23.02	1	0.19
PG 1211+143	0.081	8.7	17	12.3	33	20.3	38	33.60	80	52.60	120	127.85	320	272	2	22.53	3	24.65
PG 1216+069	0.331	2.3	8	2.6	10	3.2	8	7.47	20	9.75	20	16.05	40	24	1	23.81	3	1.65
PG 1229+204	0.063	4.6	19	6.1	28	9.2	30	13.16	30	18.66	40	56.38	120	158	1	22.40	2	0.11
PG 1244+026	0.048	1.9	8	2.5	10	3.5	12	6.89	10	10.18	20	40.80	100	114	1	22.05	3	0.53
PG 1259+593	0.478	1.9	5	2.6	8	3.9	10	9.14	20	13.58	30	18.69	40	23	1	22.59	1	0.10
PG 1302-102	0.278	3.2	8	3.5	11	4.8	12	8.80	20	13.63	30	36.74	80	103	1	26.48	1	187.00
PG 1307+085	0.155	3.5	7	4.2	11	7.1	17	9.54	20	13.52	30	32.23	70	76	1	22.59	1	0.10
PG 1309+355	0.183	3.3	7	3.6	10	5.8	13	10.41	20	16.18	30	42.22	90	117	1	24.57	3	18.00
PG 1310-108	0.034	3.9	15	4.7	19	6.4	20	10.73	20	17.29	40	63.96	130	139	1	21.09	1	0.10
PG 1322+659	0.168	1.9	6	2.6	8	4.8	12	7.81	20	11.61	20	22.38	50	48	1	22.42	1	0.12
PG 1341+258	0.087	2.0	7	2.8	11	3.9	11	7.24	10	8.82	20	19.39	40	46	1	21.21	1	0.12
PG 1351+236	0.055	5.2	15	6.4	26	7.4	22	7.91	20	7.69	20	24.91	50	56	1	22.00	3	0.26
PG 1351+640	0.088	6.4	13	7.4	22	11.9	25	25.35	60	38.46	80	149.38	360	457	3	23.68	3	4.32
PG 1352+183	0.152	1.6	5	2.1	7	3.7	9	7.22	10	10.09	20	17.88	40	35	1	22.42	1	0.11
PG 1354+213	0.300	0.7	3	1.1	6	1.6	7	3.55	10	5.31	10	12.09	30	32	1	21.96	1	0.08
PG 1402+261	0.164	2.7	7	4.6	9	9.1	18	19.95	40	28.99	60	59.20	130	115	1	22.68	3	0.23
PG 1404+226	0.098	1.9	6	2.5	8	3.8	8	5.86	10	7.74	10	17.33	40	32	1	22.71	3	0.47
PG 1411+442	0.090	7.6	14	10.3	19	16.7	30	30.36	70	44.85	100	86.36	220	134	1	22.66	3	0.13

Table 3 — *Continued*

Name	z	J [mJy]	σ J [μ Jy]	H [mJy]	σ H [μ Jy]	Ks [mJy]	σ Ks [μ Jy]	F _{3.4μm} [mJy]	σ [μ Jy]	F _{4.6μm} [mJy]	σ [μ Jy]	F _{12μm} [mJy]	σ [μ Jy]	F _{22μm} [mJy]	σ [mJy]	L _{1.4GHz} Log [W/m ²]	Ref. ^a	R ^b
PG 1415+451	0.114	2.4	6	3.0	7	4.8	12	11.79	30	19.92	40	40.84	90	78	1	22.47	3	0.17
PG 1416-129	0.129	3.7	8	5.5	13	8.5	18	10.45	20	13.57	30	28.86	60	65	1	23.43	1	1.15
PG 1425+267	0.364	1.1	5	1.4	6	3.1	10	4.47	10	6.14	10	11.91	30	30	1	25.22	3	53.60
PG 1426+015	0.086	9.7	29	14.1	48	23.8	62	28.89	70	38.49	80	94.78	230	205	1	22.52	3	0.28
PG 1427+480	0.221	1.3	5	1.7	7	2.5	9	4.75	10	7.60	10	18.40	40	47	1	21.67	1	0.16
PG 1435-067	0.126	1.3	4	1.7	7	2.7	8	3.68	10	5.68	10	13.88	30	46	1	22.13	1	0.07
PG 1440+356	0.079	10.7	21	16.2	32	25.1	43	36.27	80	44.94	100	81.12	200	193	1	22.68	3	0.37
PG 1448+273	0.065	5.6	13	7.2	16	10.1	22	11.41	20	15.23	30	44.86	100	117	1	22.55	3	0.25
PG 1501+106	0.036	9.7	27	12.8	38	17.2	45	26.03	60	36.76	80	160.81	390	445	3	21.90	1	0.36
PG 1512+370	0.371	2.5	7	3.2	10	5.8	15	7.72	20	12.04	20	24.84	50	41	1	25.44	3	190.00
PG 1519+226	0.137	1.1	4	1.3	6	2.2	9	4.22	10	6.73	10	13.70	30	34	1	23.10	1	0.90
PG 1534+580	0.030	5.7	16	7.0	22	8.9	23	20.06	40	26.34	50	74.46	170	188	1	22.02	3	0.70
PG 1535+547	0.039	6.2	13	9.4	20	14.8	28	26.08	60	32.76	70	52.71	110	82	1	21.61	3	0.14
PG 1543+489	0.400	2.3	5	3.8	8	6.8	13	12.13	30	17.12	30	35.21	80	66	1	23.98	3	0.15
PG 1545+210	0.264	1.9	6	2.2	8	3.5	10	7.90	20	11.34	20	17.26	40	38	1	25.94	3	418.00
PG 1552+085	0.119	1.3	4	2.0	6	3.7	9	8.04	20	12.55	20	38.29	80	32	1	22.70	1	0.45
PG 1612+261	0.131	2.9	8	3.5	9	5.4	14	8.56	20	10.81	20	19.53	50	31	1	23.86	3	2.81
PG 1613+658	0.129	8.6	24	10.4	41	18.1	52	25.89	60	37.90	80	91.26	200	207	1	23.19	2	1.00
PG 1617+175	0.112	2.9	7	3.9	10	7.2	13	18.23	40	24.02	50	36.77	90	55	1	22.78	1	0.72
PG 1626+554	0.133	2.8	8	3.4	10	5.7	14	9.25	20	12.02	20	16.15	30	20	1	22.13	1	0.11
PG 1700+518	0.292	3.0	8	4.3	13	7.5	13	11.32	20	14.41	30	35.83	70	106	1	24.69	3	2.36
PG 1704+608	0.372	3.5	8	4.2	12	7.1	16	15.29	30	22.44	50	37.52	70	108	1	26.24	3	645.00
PG 2112+059	0.466	4.7	9	6.4	13	10.8	19	24.29	50	36.32	80	83.70	180	194	1	24.03	1	0.32
PG 2130+099	0.063	11.7	30	20.5	52	36.0	71	48.12	120	68.52	170	154.99	400	333	2	22.67	3	0.32
PG 2209+184	0.070	4.0	14	4.9	22	6.4	22	10.96	20	13.22	30	19.09	50	23	1	23.95	2	141.00
PG 2214+139	0.066	7.8	25	11.7	35	19.4	41	39.84	100	49.91	110	70.71	170	108	1	21.65	1	0.05
PG 2233+134	0.326	1.0	4	1.2	5	2.0	9	5.30	10	8.41	20	20.49	50	56	1	23.42	1	0.28
PG 2251+113	0.326	2.7	7	4.2	11	6.6	15	12.61	20	16.21	30	23.94	60	49	1	26.21	3	365.00
PG 2304+042	0.042	3.9	18	5.0	29	6.4	23	8.17	20	7.81	10	14.17	40	30	1	21.75	1	0.25
PG 2308+098	0.433	2.4	5	2.8	8	3.4	6	5.75	10	8.73	20	13.23	40	24	1	25.49	3	188.00

^a 1: FIRST survey (Becker et al. 1995), 2: NVSS survey (Condon 1992), 3: data published in Kellermann et al. (1989)

^b Radio Loudness as described in section 3.5, introduced and measured by Kellermann et al. (1989).

Table 4
Rest Frame Luminosities from MIR and FIR photometry with Herschel and WISE

Name	$\nu L_{\nu 5.5\mu m}$ Log(L _⊙)	$\nu L_{\nu 8\mu m}$ Log(L _⊙)	$\nu L_{\nu 24\mu m}$ Log(L _⊙)	$\nu L_{\nu 60\mu m}$ Log(L _⊙)	$\nu L_{\nu 70\mu m}$ Log(L _⊙)	$\nu L_{\nu 100\mu m}$ Log(L _⊙)	$\nu L_{\nu 160\mu m}$ Log(L _⊙)	$\nu L_{\nu 250\mu m}$ Log(L _⊙)	$\nu L_{\nu 350\mu m}$ Log(L _⊙)	$\nu L_{\nu 500\mu m}$ Log(L _⊙)	L_{FIR1}^a Log(L _⊙)	L_{FIR}^b Log(L _⊙)
PG 0003+158	11.9	11.9	11.8	11.4	11.3	<12.6	< 10.9	<12.2	<12.0	<11.9	< 12.1	...
PG 0003+199	10.4	10.2	10.2	9.8	9.7	9.4	8.9	8.5	8.1	< 7.8	9.8	9.7
PG 0007+106	11.0	10.9	11.0	10.7	10.7	10.6	10.3	10.0	9.8	9.7	10.7	10.7
PG 0026+129	11.2	11.1	10.9	10.2	10.1	<11.4	< 9.8	<11.0	<10.9	<10.7	< 11.0	...
PG 0043+039	11.9	11.8	11.7	11.6	11.6	11.4	11.4	10.7	< 10.4	<11.7	11.6	11.5
PG 0049+171	10.1	10.0	9.8	9.7	9.7	9.4	9.2	< 8.8	<10.1	<10.0	9.7	9.6
PG 0050+124	11.3	11.3	11.5	11.4	11.3	11.2	10.9	10.3	9.8	9.2	11.3	11.3
PG 0052+251	11.3	11.2	11.2	10.8	10.8	10.8	10.6	10.2	9.8	< 9.5	10.8	10.8
PG 0157+001	11.5	11.6	12.2	12.3	12.3	12.0	11.6	11.0	10.4	9.9	12.3	12.2
PG 0804+761	11.5	11.4	11.2	10.7	10.5	10.0	9.5	< 9.2	<10.6	<10.4	10.6	10.6
PG 0838+770	10.9	10.9	11.1	11.0	10.9	10.9	10.7	10.2	9.7	< 9.3	11.0	10.9
PG 0844+349	10.6	10.5	10.5	9.9	9.8	10.0	10.1	9.4	9.0	8.7	10.0	10.1
PG 0921+525	10.2	10.1	10.0	9.6	9.5	9.5	9.0	8.7	8.2	< 8.1	9.6	9.6
PG 0923+129	10.0	10.1	10.2	10.2	10.2	10.2	9.9	9.3	8.8	8.4	10.3	10.3
PG 0923+201	11.6	11.5	11.2	10.8	10.7	<11.7	< 10.0	<11.3	< 9.7	<11.0	< 11.3	10.6
PG 0934+013	9.9	10.0	10.3	10.2	10.2	10.1	9.9	< 8.7	< 9.9	< 9.8	10.2	10.2
PG 0947+396	11.5	11.4	11.4	11.3	11.2	11.3	11.1	10.7	10.2	< 9.8	11.3	11.3
PG 0953+414	11.8	11.6	11.3	10.7	10.6	10.3	10.1	9.8	< 9.9	<11.2	10.6	10.5
PG 1001+054	11.2	11.1	11.0	10.7	10.6	10.2	9.6	< 9.7	<11.0	<10.8	10.6	10.6
PG 1004+130	11.6	11.7	11.7	11.4	11.4	11.1	10.4	10.3	< 9.9	<11.2	11.3	11.3
PG 1011-040	10.3	10.3	10.5	10.2	10.2	10.2	9.9	9.4	8.9	< 8.6	10.2	10.2
PG 1012+008	11.4	11.3	11.3	11.0	10.9	10.8	10.5	10.2	9.9	< 9.7	11.0	10.9
PG 1022+519	10.0	9.9	9.9	10.1	10.1	10.0	9.7	9.2	8.7	< 9.8	10.1	10.1
PG 1048+342	10.9	10.9	10.9	10.6	10.6	10.9	10.9	10.2	9.9	< 9.6	10.8	10.8
PG 1048-090	11.7	11.5	11.5	11.1	11.1	<12.3	< 10.5	<11.9	<11.8	<11.6	< 11.9	11.0
PG 1049-005	12.0	11.9	11.8	12.2	12.2	11.8	11.3	11.1	10.7	< 10.3	12.1	12.0
PG 1100+772	11.9	11.8	11.8	11.7	11.7	11.4	11.2	< 10.4	<11.6	<11.5	11.6	11.5
PG 1103-006	12.2	12.0	11.8	11.5	11.5	<12.5	< 10.9	<12.1	<12.0	<11.8	< 12.1	...
PG 1114+445	11.4	11.3	11.4	10.8	10.7	10.4	10.1	< 8.5	<10.9	<10.7	10.7	10.7
PG 1115+407	11.1	11.1	11.1	11.1	11.1	11.2	10.9	10.5	9.9	< 9.5	11.2	11.2
PG 1116+215	11.8	11.7	11.5	11.0	10.9	10.5	10.0	9.8	< 9.7	<10.9	10.9	10.7
PG 1119+120	10.4	10.5	10.7	10.5	10.4	10.2	10.0	9.3	8.6	< 8.4	10.4	10.4
PG 1121+422	11.2	11.1	10.9	<12.1	<10.4	<11.9	<11.7	<11.5	<11.3	<11.2	< 12.1	...
PG 1126-041	10.9	10.8	10.9	10.8	10.8	10.6	10.3	9.7	9.1	8.7	10.8	10.7
PG 1149-110	10.1	10.1	10.4	10.3	10.3	10.1	9.9	9.3	8.9	8.4	10.3	10.3
PG 1151+117	11.1	11.0	10.9	10.6	10.4	<11.6	< 10.0	<11.2	<11.1	<10.9	< 11.2	...
PG 1202+281	11.2	11.1	11.3	10.9	10.9	10.7	10.3	10.0	9.6	9.3	10.9	10.8
PG 1211+143	11.2	11.1	11.1	10.4	10.3	9.9	9.4	8.9	8.9	8.6	10.3	10.3
PG 1216+069	11.8	11.7	11.4	11.0	10.9	<12.3	< 10.6	<11.9	<11.7	<11.6	< 11.8	...
PG 1229+204	10.5	10.5	10.7	10.3	10.2	10.2	9.9	9.5	9.0	< 8.7	10.3	10.3
PG 1244+026	10.0	10.1	10.3	10.1	10.0	9.8	9.4	8.9	8.5	< 8.5	10.0	10.0
PG 1259+593	12.3	12.2	11.7	11.1	11.0	<12.6	< 11.0	<12.2	<12.1	<11.9	< 12.2	...
PG 1302-102	11.8	11.8	11.9	11.6	11.5	11.4	11.3	11.1	11.0	11.0	11.5	11.1
PG 1307+085	11.2	11.2	11.1	10.5	10.5	10.4	9.9	< 9.6	<11.0	<10.8	10.5	10.5
PG 1309+355	11.5	11.4	11.5	11.0	10.9	10.7	10.4	10.0	9.4	< 9.7	10.9	10.9
PG 1310-108	9.9	10.0	10.0	9.5	9.4	9.3	9.0	8.6	8.3	< 8.2	9.5	9.5
PG 1322+659	11.2	11.1	11.1	11.0	11.0	10.9	10.5	10.0	< 9.5	<10.9	11.0	11.0
PG 1341+258	10.4	10.4	10.5	10.3	10.2	10.1	9.7	9.4	8.9	< 9.0	10.2	10.2
PG 1351+236	10.0	10.0	10.2	10.5	10.5	10.4	10.1	9.7	9.1	8.2	10.5	10.5
PG 1351+640	11.2	11.2	11.5	11.2	11.1	10.9	10.4	9.4	< 10.4	<10.3	11.1	11.1
PG 1352+183	11.0	10.9	10.8	10.3	10.2	9.9	9.6	< 9.7	<10.9	<10.8	10.2	10.1
PG 1354+213	11.5	11.4	11.5	11.3	11.2	10.9	10.6	< 10.3	<11.6	<11.5	11.2	11.0
PG 1402+261	11.6	11.5	11.5	11.4	11.3	11.1	10.6	10.2	9.7	9.3	11.3	11.3

Table 4 — *Continued*

Name	$\nu L_{\nu 5.5\mu\text{m}}$ Log(L_{\odot})	$\nu L_{\nu 8\mu\text{m}}$ Log(L_{\odot})	$\nu L_{\nu 24\mu\text{m}}$ Log(L_{\odot})	$\nu L_{\nu 60\mu\text{m}}$ Log(L_{\odot})	$\nu L_{\nu 70\mu\text{m}}$ Log(L_{\odot})	$\nu L_{\nu 100\mu\text{m}}$ Log(L_{\odot})	$\nu L_{\nu 160\mu\text{m}}$ Log(L_{\odot})	$\nu L_{\nu 250\mu\text{m}}$ Log(L_{\odot})	$\nu L_{\nu 350\mu\text{m}}$ Log(L_{\odot})	$\nu L_{\nu 500\mu\text{m}}$ Log(L_{\odot})	L_{FIR1}^a Log(L_{\odot})	L_{FIR}^b Log(L_{\odot})
PG 1404+226	10.5	10.5	10.4	10.3	10.2	10.1	10.0	9.6	9.3	< 9.1	10.2	10.2
PG 1411+442	11.2	11.1	10.9	10.4	10.3	10.3	10.0	9.6	9.3	8.8	10.4	10.4
PG 1415+451	11.1	11.0	10.9	10.7	10.7	10.6	10.1	9.8	< 9.2	< 10.5	10.7	10.7
PG 1416-129	11.0	10.9	10.9	10.4	10.3	10.0	9.8	< 9.5	< 10.8	< 10.6	10.3	10.3
PG 1425+267	11.7	11.7	11.8	11.7	11.7	11.1	10.2	< 10.5	< 11.8	< 11.7	11.6	11.5
PG 1426+015	11.1	11.1	11.1	10.8	10.8	10.7	10.4	< 10.6	< 10.4	< 10.3	10.8	10.8
PG 1427+480	11.3	11.3	11.4	11.1	11.1	10.7	10.4	10.1	< 9.8	< 11.2	11.1	11.0
PG 1435-067	10.6	10.6	10.7	< 9.9	< 9.9	< 9.6	< 11.1	< 10.9	< 9.3	< 10.6	12.4	...
PG 1440+356	11.0	10.9	11.0	11.1	11.1	11.0	10.6	10.1	9.5	9.0	11.1	11.1
PG 1448+273	10.4	10.4	10.6	10.3	10.2	10.1	9.9	9.2	8.8	< 8.6	10.3	10.2
PG 1501+106	10.3	10.4	10.6	10.2	10.1	9.9	9.6	< 8.3	< 9.6	< 9.5	10.1	10.1
PG 1512+370	12.0	12.0	11.7	11.2	11.1	11.0	10.9	10.4	< 10.4	< 11.7	11.2	11.0
PG 1519+226	10.8	10.7	10.8	10.6	10.6	10.6	10.3	< 9.6	< 10.9	< 10.7	10.7	10.6
PG 1534+580	10.0	9.9	10.1	9.6	9.6	9.5	9.3	8.5	8.1	< 8.0	9.6	9.6
PG 1535+547	10.2	10.1	9.9	9.5	9.4	9.2	9.0	8.7	8.3	< 8.2	9.4	9.4
PG 1543+489	12.3	12.2	12.3	12.4	12.4	12.0	11.7	11.2	10.7	< 10.5	12.3	12.2
PG 1545+210	11.6	11.5	11.3	< 10.6	< 10.6	< 10.3	< 11.8	< 11.6	< 10.0	< 11.3	13.3	...
PG 1552+085	10.9	11.1	10.6	10.2	10.2	10.1	9.6	< 9.4	< 10.7	< 10.6	10.2	10.2
PG 1612+261	10.9	10.8	10.8	11.1	11.1	10.9	10.7	10.1	9.5	< 9.3	11.1	11.1
PG 1613+658	11.5	11.4	11.5	11.6	11.6	11.5	11.2	10.7	10.1	9.5	11.6	11.6
PG 1617+175	11.1	11.0	10.7	10.1	10.1	< 11.2	< 9.6	< 10.8	< 10.7	< 10.5	< 10.8	...
PG 1626+554	10.9	10.8	10.5	< 11.6	< 9.9	< 11.4	< 11.2	< 11.0	9.6	9.4	< 11.5
PG 1700+518	11.9	11.9	12.1	12.2	12.2	11.8	11.5	11.0	10.5	9.9	12.1	12.0
PG 1704+608	12.3	12.2	12.3	12.0	12.0	11.6	11.3	10.9	10.4	< 10.3	11.9	11.9
PG 2112+059	12.8	12.8	12.6	11.9	11.8	11.7	11.6	< 10.8	< 12.1	< 11.9	11.9	11.7
PG 2130+099	11.0	11.0	11.0	10.7	10.7	10.5	10.3	9.7	9.2	8.8	10.7	10.7
PG 2209+184	10.4	10.3	10.0	9.9	9.9	10.1	10.0	9.6	9.3	9.1	10.0	10.1
PG 2214+139	10.9	10.8	10.5	9.9	9.8	9.8	9.7	9.2	9.0	8.6	9.9	9.9
PG 2233+134	11.8	11.8	11.8	11.4	11.3	11.0	10.6	< 10.4	< 11.7	< 11.5	11.3	11.2
PG 2251+113	12.0	11.9	11.7	11.3	11.2	< 12.2	< 10.6	< 11.8	< 11.7	< 11.5	< 11.8	...
PG 2304+042	9.7	9.6	9.6	9.1	9.0	< 10.3	< 8.7	< 9.9	< 9.8	< 9.6	< 9.9	8.8
PG 2308+098	12.0	11.9	11.7	11.1	11.0	< 12.5	< 10.9	< 12.1	< 12.0	< 11.8	< 12.1	...

^a L_{FIR} [42.5-122.5 μm] as defined in Helou et al. (1985)^b L_{FIR} [40-500 μm] integrated over the best modified black body fit.

Table 5
Basic Statistics of IR Luminosities

Restframe Luminosity	Minimum Detection [L _⊙]	Maximum Detection [L _⊙]	Median Detection [L _⊙]	Kaplan-Meier Median [L _⊙]	95% confidence interval [L _⊙]
L _{60μm}	1.4×10^9	2.8×10^{13}	6×10^{10}	6×10^{10}	$4 - 10 \times 10^{10}$
L _{100μm}	1.5×10^9	1.0×10^{12}	2×10^{10}	3×10^{10}	$2 - 5 \times 10^{10}$
L _{160μm}	5×10^7	4.5×10^{11}	2×10^{10}	1×10^{10}	$0.8 - 2 \times 10^{10}$
L _{250μm}	3×10^8	2.6×10^{11}	6×10^9	4×10^9	$2 - 9 \times 10^9$
L _{350μm}	1×10^8	1.1×10^{11}	3×10^9	1×10^9	$0.9 - 3 \times 10^9$
L _{500μm}	2×10^8	1.1×10^{11}	9×10^9	4×10^8	$2 - 7 \times 10^8$

Table 6
Normalized Templates at 6 μm

λ_{rest}	F_{median}	95% Interval
1.1	0.15	0.13 - 0.17
1.5	0.21	0.19 - 0.23
2.0	0.32	0.28 - 0.34
3.0	0.55	0.51 - 0.58
4.1	0.73	0.70 - 0.75
10.4	1.51	1.45 - 1.61
19.0	3.20	2.97 - 3.74
60.8	4.63	3.26 - 5.88
87.2	5.06	3.61 - 6.52
138.1	3.76	2.05 - 5.71
217.6	1.60	0.90 - 2.31
308.4	0.80	0.73 - 1.34
436.0	0.46	0.25 - 0.68

Table 7
Cold Dust Estimates

Name	$\log(M1_D)^a$ [M_\odot]	$T1_D$ [K] $\beta = 1.91$	Fitting Errors	$\log(M2_D)^b$ [M_\odot]	$T2_D$ [K] $\beta = 2.08$	Fitting Errors
PG 0043+039	6.9	36	12%	7.0	35	12%
PG 0049+171	5.2	37	22%	5.3	36	22%
PG 0050+124	7.3	32	0%	7.4	30	0%
PG 0052+251	7.2	26	6%	7.4	25	6%
PG 0157+001	7.6	40	1%	7.7	38	1%
PG 0804+761	5.0	66	8%	5.1	61	8%
PG 0838+770	7.2	28	3%	7.3	26	3%
PG 0844+349	6.8	23	5%	6.9	22	5%
PG 0921+525	6.0	27	5%	6.1	25	5%
PG 0923+129	6.5	28	1%	6.7	27	1%
PG 0923+201	6.3	34	20%	6.4	32	20%
PG 0934+013	6.0	33	4%	6.1	32	4%
PG 0947+396	7.6	26	4%	7.7	25	4%
PG 0953+414	6.3	33	23%	6.4	31	23%
PG 1001+054	5.3	53	20%	5.4	50	20%
PG 1004+130	6.6	39	8%	6.7	38	8%
PG 1011-040	6.6	26	3%	6.8	25	3%
PG 1012+008	7.1	28	8%	7.2	27	8%
PG 1022+519	6.4	28	3%	6.6	27	3%
PG 1048+342	7.3	25	6%	7.4	24	6%
PG 1048-090	6.0	43	8%	6.0	43	8%
PG 1049-005	6.8	48	4%	6.8	47	4%
PG 1100+772	6.1	54	2%	6.2	52	2%
PG 1115+407	7.4	27	3%	7.6	26	3%
PG 1116+215	6.2	37	8%	6.3	35	8%
PG 1119+120	6.2	34	2%	6.3	33	2%
PG 1126-041	6.7	32	2%	6.8	30	2%
PG 1149-110	6.4	29	2%	6.6	28	2%
PG 1202+281	6.8	30	8%	7.0	29	8%
PG 1229+204	6.7	27	4%	6.8	26	4%
PG 1244+026	5.8	34	5%	6.0	32	5%
PG 1307+085	6.0	37	15%	6.1	36	15%
PG 1309+355	6.1	42	5%	6.2	41	5%
PG 1310-108	5.9	27	7%	6.0	26	7%
PG 1322+659	6.6	35	5%	6.8	33	5%
PG 1341+258	6.3	30	8%	6.4	29	8%
PG 1351+236	6.8	28	2%	6.9	27	2%
PG 1351+640	6.3	43	2%	6.4	41	2%
PG 1352+183	5.3	42	17%	5.4	40	18%
PG 1354+213	6.0	45	8%	6.1	44	8%
PG 1402+261	6.8	37	3%	6.9	35	3%
PG 1404+226	6.9	23	7%	7.1	22	7%
PG 1411+442	6.8	26	5%	7.0	25	5%
PG 1415+451	6.7	30	6%	6.8	29	6%
PG 1416-129	5.3	46	11%	5.4	44	11%
PG 1425+267	5.8	62	12%	5.8	59	12%
PG 1426+015	6.5	35	3%	6.5	34	3%
PG 1427+480	6.4	38	12%	6.5	37	12%
PG 1440+356	7.0	32	1%	7.1	31	1%
PG 1448+273	6.3	31	5%	6.4	29	5%
PG 1501+106	5.5	41	3%	5.6	40	3%
PG 1512+370	6.8	31	21%	6.9	30	21%
PG 1519+226	6.5	32	11%	6.6	31	11%
PG 1534+580	5.6	31	5%	5.8	30	5%
PG 1535+547	6.2	23	9%	6.3	22	9%
PG 1543+489	7.2	44	3%	7.2	42	3%
PG 1552+085	5.8	35	5%	5.9	34	5%
PG 1612+261	6.9	33	4%	7.0	31	4%
PG 1613+658	7.5	31	1%	7.7	30	1%
PG 1700+518	7.3	40	2%	7.4	38	2%
PG 1704+608	6.8	45	5%	6.9	43	5%
PG 2112+059	6.2	54	11%	6.3	52	11%
PG 2130+099	6.7	31	2%	6.8	30	2%
PG 2214+139	6.6	24	6%	6.7	23	6%
PG 2233+134	6.0	49	17%	6.1	46	17%
PG 2304+042	6.6	15	19%	6.7	15	19%

^a Values determined from modified blackbody fits, with absorption coefficients and spectral indices derived from the dust model of (Compiègne et al. 2011).

^b Values determined from modified blackbody fits, with absorption coefficients and spectral indices derived from the dust model of (Draine & Li 2007)

